Distinguishing volcanic contributions to the overlapping Samoan and Cook-Austral hotspot tracks

Allison A Price, Matthew G Jackson, Janne Blichert-Toft, Kevin Konrad, Michael Bizimis, Anthony a P Koppers, Jasper G Konter, Valerie A Finlayson, John M Sinton

Distinguishing volcanic contributions to the overlapping Samoan and Cook-Austral hotspot tracks

Allison A. Price[1*], Matthew G. Jackson[1], Janne Blichert-Toft[2], Kevin Konrad[3], Michael Bizimis[4], Anthony A.P. Koppers[5], Jasper G. Konter[6], Valerie A. Finlayson[7], John M. Sinton[6]

[1] Department of Earth Science, University of California Santa Barbara, California 93106, USA
[2] Ecole Normale Supérieure de Lyon, CNRS, Université de Lyon, Lyon, France
[3] Department of Geoscience, University of Nevada Las Vegas, Las Vegas, Nevada 89154, USA
[4] School of Earth, Ocean and Environment, University of South Carolina, Columbia, South Carolina 29208, USA
[5] College of Earth, Ocean and Atmospheric Sciences, Oregon State University, Corvallis, Oregon 97331 USA
[6] Department of Earth Sciences, School of Ocean and Earth Science and Technology, University of Hawai‘i Mānoa, Honolulu, Hawaii 96822 USA
[7] Department of Geology, University of Maryland College Park, College Park, Maryland 20742

*Corresponding author. Phone: (925) 285-4561. E-mail: price@ucsb.edu

ABSTRACT

To deconvolve contributions from the four overlapping hotspots that form the “hotspot highway” on the Pacific plate—Samoa, Rarotonga, Arago-Rurutu, and Macdonald—we geochemically characterize and/or date (by the $^{40}Ar/^{39}Ar$ method) a suite of lavas sampled from the “downstream” Samoan hotspot track. We find that Papatua seamount, located ~60 km south of the axis of the Samoan hotspot track, has lavas with both a HIMU composition ($^{206}Pb/^{204}Pb$ =

20.0), previously linked to one of the Cook-Austral hotspots, and an EM1 composition, which we interpret to be rejuvenated and Samoan in origin. We show that these EM1 rejuvenated lavas are geochemically similar to rejuvenated volcanism on Samoan volcanoes, and suggest that flexural uplift, caused by tectonic forces associated with the nearby Tonga trench, triggered a new episode of melting of Samoan mantle material that had previously flattened and spread laterally along the base of the Pacific plate under Papatua, resulting in volcanism that capped the previous HIMU edifice. We argue that this process generated Samoan rejuvenated volcanism on the older Cook-Austral volcano of Papatua. We also study Waterwitch seamount, located ~820 km WNW of the Samoan hotspot, and provide an age (10.49 ± 0.09 Ma) which places it on the Samoan hotspot trend, showing that it is genetically Samoan and not related to the Cook-Austral hotspots as previously suggested. Consequently, with the possible exception of the HIMU stage of Papatua seamount, there are currently no known Arago-Rurutu plume-derived lava flows sampled along the swath of Pacific seafloor that stretches between Rose seamount (~25 Ma) and East Niulakita seamount (~45 Ma), located 1400 km to the west. The “missing” ~20-million-year segment of the Arago-Rurutu hotspot track may have been subducted into the northern Tonga trench, or perhaps was covered by subsequent volcanism from the overlapping Samoan hotspot,

and has thus eluded sampling. Finally, we explore tectonic reactivation as a cause for anomalously young volcanism present within the western end of the Samoan hotspot track.

KEYWORDS

Cook-Austral; Samoa; OIB; geochemistry; OIB; radiogenic isotopes

INTRODUCTION

Hotspots are generally thought to be formed by upwelling mantle plumes that melt beneath an overriding plate, which produces a hotspot track, a series of age-progressive volcanoes that extend linearly away from the volcanically active hotspot (e.g. Morgan, 1971, 1972). The so-called "hotspot highway" in the south Pacific results from four overlapping hotspot tracks—Macdonald, Arago-Rurutu, Rarotonga, and Samoa—that lie on the same Pacific plate flowline (e.g. Duncan and McDougall 1976; Turner and Jarrard, 1982; Matsuda et al.,1984; Diraison, 1991; Chauvel et al., 1997; McNutt et al.,1997; Bonneville et al., 2002; Bonneville et al., 2006; Konter et al., 2008; Jackson et al., 2010; Maury et al., 2013; Finlayson et al., 2018; Jackson et al., 2020; Buff et al., 2021) (Figure 1). The "downstream" Samoan hotspot track in the hotspot

highway is anchored on the young end by the volcanically active Vailulu‘u seamount, and extends towards older volcanoes in the west that reach 24 Ma ages (Figures 1, 2). The Samoan hotspot track is divided into two provinces: 1) the Eastern Samoan Volcanic Province (ESAM), which is bracketed on the east end by the volcanically active Vailulu‘u seamount and extends ~350 km to the west to Savai‘i (5.29 Ma; Koppers et al., 2008) (Hart et al., 2000; Staudigel et al., 2004, 2006); and 2) the Western Samoan Volcanic Province (WESAM), which consists of older Samoan volcanoes that lie to the west of Savai‘i and extend westward to Alexa bank (23.96 Ma; Hart et al., 2004), located ~1300 km west of Savai‘i Island (e.g. Hawkins and Natland, 1975; Duncan, 1985; Sinton et al., 1985; Johnson et al., 1986; Jackson et al., 2010) (Figures 1, 2). Samoan lavas can exhibit high $^{3}He/^{4}He$ signatures, up to 34 R_A (where R_A is the measured ratio relative to atmosphere; Jackson et al., 2007a) or strong enriched mantle II (EM2) compositions characterized by high $^{87}Sr/^{86}Sr$ (up to 0.723888 ± 0.000015 [2SE] in magmatic clinopyroxene; Adams et al., 2021), although we note that high $^{3}He/^{4}He$ and high $^{87}Sr/^{86}Sr$ are not typically found in the same samples (e.g. Jackson et al., 2007a). Samoan lavas can also exhibit geochemical characteristics that are associated with dilute contributions from three other canonical mantle endmembers—enriched mantle I (EM1), HIMU (high $\mu = {}^{238}U/^{204}Pb$), and a

depleted component (DM) (e.g. Jackson et al., 2014).

Along the Samoan hotspot track, several volcanoes occur "off axis" and are displaced to the south of the main hotspot trace. For example, Papatua seamount is located ~60 km south of the Samoan island of Tutuila. Jackson et al. (2010) presented data for a Papatua lava (sample ALIA-D129-05, dredged at 2518 to 2408 meters below sea level (mbsl)) with a HIMU geochemical composition, which they interpreted to be of non-Samoan origin and potentially related to one of the Cook-Austral hotspots. They argued that the HIMU flavor in this lava, along with the thick (>5 cm) ferromanganese rind attached to the Papatua sample (which contrasts with the thin [<1 mm] ferromanganese patinas on submarine samples from nearby Samoan volcanoes), is evidence that Papatua was erupted over one of the HIMU Cook-Austral hotspots that lie ~2180 km (Arago-Rurutu hotspot) to ~3390 km (Macdonald hotspot) ESE of the Samoan hotspot. In support of this hypothesis, volcanic seamounts comprising older portions of the Cook-Austral hotspot tracks have been found in the vicinity of the Samoan hotspot track. For example, Rose atoll (24.8 ± 1 Ma; Buff et al., 2021), located adjacent to Vailulu'u seamount, relates to the Arago-Rurutu hotspot (Figures 1, 2). Malulu seamount, which lies between Rose atoll and Vailulu'u seamount (Figures 1, 2), has a HIMU composition and therefore likely relates to either

the Arago-Rurutu or Macdonald hotspot (but ages are not available for Malulu, hence a specific designation cannot be made; Buff et al., 2021). Located north of Vailulu'u, the HIMU Moki seamount (44.53 ± 10.05 Ma; Buff et al., 2021) relates to the Macdonald hotspot (Figures 1, 2). At the older end of the Samoan hotspot track, East Niulakita seamount has been shown to host both older HIMU Arago-Rurutu lavas (42.24 ± 0.82 Ma to 45.73 ± 0.14 Ma; Finlayson et al., 2018) and younger shield-stage Samoan lavas (14.76 ± 0.12 Ma; Finlayson et al., 2018) (Figures 1, 2). It is evident that volcanoes in the Samoan region must be distinguished by age and/or geochemical composition to determine their hotspot of origin, as Cook-Austral hotspot volcanoes in the Samoan region have older ages and different geochemical compositions than Samoan hotspot volcanoes.

Here we report geochemical and isotopic data and $^{40}Ar/^{39}Ar$ ages on selected lavas from eight submarine volcanoes located in the Samoan region: the dataset includes 12 lavas from seven volcanoes in the WESAM region (including new $^{40}Ar/^{39}Ar$ ages on four samples), as well as geochemical data on two glasses from Papatua seamount. Using the data, we explore three significant findings: First, we evaluate whether old volcanoes from the Cook-Austral hotspots can be traced into the WESAM region of the Samoan hotspot track. Second, we investigate the

106 origins of the two stages of volcanism at Papatua seamount. Lastly, we examine the causes of
107 rejuvenated volcanism at Papatua and along the WESAM portion of the Samoan hotspot.
108
109 **Sample location and descriptions**
110 The samples in this study were recovered during four separate dredging expeditions: samples
111 with prefix KK8203 were collected during the 1982 KK820316 cruise of the *R/V Kana Keoki*;
112 samples with prefix PPT were collected during the 1986 Papatua Expedition of the *R/V Thomas*
113 *Washington*; one sample with prefix ALIA was collected by seafloor dredging during a 2005
114 expedition of the *R/V Kilo Moana;* samples with prefix RR1310 were recovered by seafloor
115 dredging during a 2013 expedition of the *R/V Roger Revelle*. The volcanoes sampled (and
116 presented in this study) include the Lalla Rookh, Siafiafi, Bustard, Waterwitch, Talviuni, Fa'aitu,
117 and Papatua seamounts, and Tuscarora bank (Figure 2). Only basalt clasts hosted in hyaloclastite
118 were obtained from Lalla Rookh (RR1310-D40-10), Siafiafi (ALIA-D121-09), Tuscarora
119 (KK8203-DR-9), and Talviuni (KK8203-DR-1); in these cases, only the freshest clasts were
120 separated for geochemical and isotopic analyses. In total, 14 volcanic samples from eight

121 different volcanoes were geochemically and isotopically characterized and/or dated by the
122 $^{40}Ar/^{39}Ar$ method.

123 Table 1 provides sample descriptions and locations, information about which samples
124 have new $^{40}Ar/^{39}Ar$ ages, major and trace element, and/or isotope data, as well as information
125 about prior isotopic studies of samples from the same volcanoes.

126

127 ## METHODS

128 ### $^{40}Ar/^{39}Ar$ age determination

129 New $^{40}Ar/^{39}Ar$ age determinations on four submarine lava flows are presented in Table 2. Three
130 plagioclase separates and two groundmass separates were obtained by systematic crushing,
131 sieving, magnetic separation, acid leaching, and handpicking as described in Konrad et al.
132 (2018). Samples were irradiated along with Fish Canyon Tuff sanidine (FCT) fluence monitors at
133 the Oregon State University (OSU) TRIGA reactor for 6 hours. Extracted gas was analyzed
134 using an ARGUS VI mass spectrometer. Samples were analyzed via the incremental heating
135 method using 21-27 CO_2 laser heating steps with blanks analyzed at the start, end, and between
136 every three heating steps. Age determinations were calculated using ArArCALC v2.7.0

(Koppers, 2002) with an FCT age of 28.201 ± 0.046 Ma (Kuiper et al., 2008) and the decay constant of Min et al. (2000). Ages were considered reliable if plateau lengths were greater than 60% of the ^{39}Ar released and probability of fit factors were > 5%. A sample with a plateau consisting of 40-60% of ^{39}Ar released is considered a mini-plateau and we interpret the corresponding age with caution.

Major and trace elements

Major element analyses of whole rock powders were conducted at Washington State University (WSU) by X-ray fluorescence spectrometry on a ThermoARL XRF following methods outlined elsewhere (Johnson and Sinton, 1990). The USGS BCR-2 reference material was run together with the samples. Measured major element concentrations for the BCR-2 analyzed here are within 1.8% of the recommended values in Jochum et al. (2016), except for P_2O_5 (3.7%), and the data are reported in Table 3. Six samples from this study—RR1310-D40-10, RR1310-D34-01, KK8203-DR-1, KK8203-DR-9, ALIA-D121-09, and RR1310-D29-01—were not measured for major element concentrations, generally owing to lack of sufficient material.

Major elements of Papatua glasses (PPT-D1-N1 and PPT-D1-N2) were measured *in situ*

by electron microprobe at UC Santa Barbara (UCSB) using primary standards and following the analytical conditions outlined in Jackson et al. (2015). The secondary MORB glass standard ALV519-4-1 was measured repeatedly throughout the analytical session (Table 4). The replicate major element analyses of ALV519-4-1 are reproducible to within 2.0% (2RSD, N=22) except for Na_2O (2.5%), K_2O (4.5%), MnO (5.2%), and P_2O_5 (19%), while the major element concentrations of ALV519-4-1 reported here agree with the Melson et al. (2002) values to within 3.2% except for K_2O (18.7%) and P_2O_5 (27.1%) (the low concentrations of these two elements, at ~0.1 wt.%, may explain the poorer agreement).

Trace element analyses on all samples, except the two Papatua glasses, were measured by ICP-MS at WSU on approximately 200 mg of whole-rock or hyaloclastite clast powder. Methods followed those described elsewhere (Knaack et al., 1994; Hart and Blusztajn, 2006). An aliquot of the USGS BCR-2 reference material was run as an unknown together with the samples to assess reproducibility. Measured trace element concentrations are within 6.8% of the recommended values in Jochum et al. (2016), except for Eu (7.1%), Tb (9.5%), Dy (8.8%), and Ho (11.4%) (Table 3). Three samples from this study, RR1310-D40-10, RR1310-D34-01, and RR1310-D29-01, were not measured for trace element concentrations.

Trace element analyses on the two Papatua glasses (PPT-D1-N1 and PPT-D1-N2) were measured using a Thermo Scientific Element XR ICP-MS coupled to a Resonetics M-50E 193 nm ArF excimer laser at Laboratoire Magmas et Volcans at Clermont-Ferrand. Samples were internally standardized using ^{43}Ca. Analytical methods followed those in Oulton et al. (2016) and Reinhard et al. (2018) except that a 47 μm laser spot fired with a 4 Hz repetition rate was used for analysis of both samples and standards. Calibration curves were generated using the NIST612 (Gagnon et al., 2008) and BCR-2 (Jochum et al., 2006) glasses. Replicate analyses of the MORB glass standard ALV519-4-1 were made throughout the analytical session to monitor and evaluate precision and accuracy. The reproducibility of the trace element analyses was better than 6.1% (2RSD, N=8) for all elements, except for U (6.9%), Pb (9.9%), Ta (7.3%), and Cs (44%). Measured concentrations are compared with previously published analyses from Melson et al. (2002) and Gale et al. (2013a, b) in Table 4.

Hafnium, Nd, Sr, and Pb chemical separation and mass spectrometry

183 The radiogenic isotopic data presented here were measured during two analytical campaigns: the
184 first at the Ecole Normale Supérieure de Lyon (ENS Lyon) and University of North Carolina
185 Chapel Hill (UNC), and the second at UCSB and University of South Carolina (USC) (Table 5).
186
187 *Analyses carried out at ENS Lyon and UNC*
188 Isotopic compositions were measured on ~200 mg of handpicked rock chips (not powders),
189 except for the two Papatua samples for which isotopic compositions were measured on glasses.
190 All samples were leached and dissolved at ENS Lyon using an aggressive leaching method
191 described in Price et al. (2016), except for the Papatua glasses, which were subjected to a lighter
192 leach (see method described in Blichert-Toft and Albarede (2009) and Price et al. (2014)). In
193 short, the aggressive leaching procedure first included a leach in 1 ml 30% Suprapur H_2O_2 for 15
194 min at 130° C, a 15 min ultrasonication step, and an additional 10 min of heating at 130° C. The
195 H_2O_2 was pipetted off and the samples rinsed twice with MilliQ H_2O. The samples were then
196 leached in 2 ml distilled 6M HCl for 1 h at 130° C, followed by 10 min of ultrasonication and 10
197 further min of heating at 130° C. The HCl was pipetted off and the samples rinsed twice with
198 MilliQ H_2O. Lastly, the samples were leached in 2 ml distilled 4M HNO_3 for 1 h at 130° C,

followed by 15 min of ultrasonication and 10 additional min of heating at 130° C. The HNO_3 was pipetted off and the samples rinsed twice with MilliQ H_2O. In contrast, the light leach consisted of leaching glass chips in 2 ml distilled 6M HCl for a total of 50 min at 120° C, including several intermittent steps of ultrasonication. The HCl was pipetted off and the samples rinsed twice with MilliQ H_2O.

Following sample dissolution in concentrated distilled HF and HNO_3 in the ratio of ~3:1, Hf and Pb were separated by column chromatography at ENS Lyon according to the protocols outlined in Blichert-Toft et al. (1997) and Blichert-Toft and Albarède (2009) and measured by MC-ICP-MS (Nu Plasma 500 HR), also at ENS Lyon. Lead isotopic compositions were corrected for instrumental mass fractionation by Tl addition (using a $^{205}Tl/^{203}Tl$ ratio of 2.38890) assuming an exponential fractionation law. The measured Pb isotopic compositions were further corrected to the NIST 981 values of Eisele et al. (2003) ($^{206}Pb/^{204}Pb = 16.9409 \pm 19$, $^{207}Pb/^{204}Pb = 15.4976 \pm 24$, and $^{208}Pb/^{204}Pb = 36.7262 \pm 86$ (2σ)) using sample-standard bracketing with NIST 981 being analyzed systematically every second sample throughout the run sessions. Instrumental mass fractionation correction of the measured Hf isotopic ratios also assumed an exponential fractionation law and a $^{179}Hf/^{177}Hf$ ratio of 0.7325. The unweighted mean $^{176}Hf/^{177}Hf$

215 of the JMC-475 Hf standard, which was run alternately with the samples, was identical within
216 error to the preferred value of 0.282163 ± 0.000009 (Blichert-Toft et al., 1997); hence no further
217 corrections were applied to the $^{176}Hf/^{177}Hf$ data obtained in this study. The wash from the Pb
218 columns containing the Sr and Nd fractions was collected in clean Savillex beakers and dried
219 down, then redissolved and split into two fractions at UNC to be measured for Sr and Nd
220 isotopes.

221 Strontium purification was carried out by column chromatography and Sr isotopic
222 compositions measured on a VG Sector 54 TIMS using the same methods as outlined in Jackson
223 et al. (2017). Instrumental mass fractionation correction assumed an exponential fractionation
224 law and a $^{86}Sr/^{88}Sr$ ratio of 0.1194. NBS987 run during the analysis of unknowns averaged
225 0.710256 ± 0.000013 (2 SD, N=4) and the Sr isotopic compositions of all lavas are corrected for
226 the offset between measured $^{87}Sr/^{86}Sr$ and preferred $^{87}Sr/^{86}Sr$ (0.710240) from each analytical
227 session. Neodymium separations were also carried out at UNC and Nd isotopic compositions
228 measured as oxides on a PhoeniX TIMS following methods outlined in Jackson et al. (2017).
229 Correction for instrumental mass fractionation assumed an exponential fractionation law and a

230 $^{146}Nd/^{144}Nd$ ratio of 0.7219. All samples were corrected for the offset between measured JNdi
231 (0.512103 ± 0.000012, 2SD, N=7) and preferred Jndi (0.512099; Garçon et al., 2018).
232 The samples processed for wet chemistry and mass spectrometry at ENS Lyon and UNC
233 were run together with the same suite of unleached USGS reference materials (BCR-2 and AGV-
234 2) as the basalt samples published in Jackson et al. (2017) and the isotopic compositions are
235 listed in Table 5 for completeness. The total procedural Pb and Hf blanks for the samples
236 processed at ENS Lyon are both <20 pg, while the Sr and Nd blanks for the samples processed at
237 UNC are <100 pg and < 50 pg, respectively.
238
239 *Analyses carried out at UCSB and USC*
240 A subset of samples reported here were analyzed (or re-analyzed) at UCSB and USC. The same
241 heavy leach method used at ENS Lyon (described above) was applied to all samples run at
242 UCSB, except RR1310-D31-01 and RR1310-D31-02, which were subjected to only the light
243 leach method because they were extremely fresh. Following sample digestion, Sr and Pb
244 separations were carried out at UCSB by two passes through 100 µl Eichrom Sr-spec columns
245 (based on Konter and Storm, 2014). Sample loading and mass spectrometry followed methods

described in Jackson et al. (2020) and are summarized here. Approximately 500 ng Sr was loaded on outgassed, zone-refined (99.999% purity, H-Cross, USA) Re filaments with TaCl emitter. Analyses were carried out on a Thermo Scientific Triton Plus TIMS housed at UCSB, employing amplifier rotation on 10^{11} ohm amplifiers and a 3.3 picoamp gainboard; 2 hour gains were run every other day (with the start of a new barrel). Each analysis lasted for 1 hour (excluding interblock heating and focusing) and approximately 20% of analysis time was devoted to baseline measurements (made with each rotation of the amplifiers). During analysis the beam was kept at or near 3 V on mass 88. Long-term reproducibility of NBS987 analyses on the UCSB Triton Plus—which had been operating at UCSB for approximately three months at the time of the new analyses reported here—was 0.710246 ± 0.000011 (N=29, 2SD). The measured Sr isotopic compositions were corrected for instrumental mass fractionation as indicated above. Sample unknowns and the USGS reference material (BCR-2) were corrected for the offset between preferred (0.710240) and measured $^{87}Sr/^{86}Sr$ of NBS987 analyzed in the same barrel.

Neodymium was purified by passing the Sr column washes through a series of columns filled with TRU- and Ln-spec ion-exchangers (following Price et al., 2014). Sample loading and mass

spectrometry followed the methods in Jackson et al. (2020) and is summarized here. Approximately 500 ng Nd aliquots were loaded on outgassed, zone-refined (99.999% purity, H-Cross, USA) Re filaments and analyzed for $^{143}Nd/^{144}Nd$ on the UCSB Triton Plus TIMS. Analyses employed amplifier rotation on the same amplifiers and gain board as described above; 2 hour gains were run every other day (with the start of a new barrel). Analyses lasted for 2 hours and baselines were run for ~20% of each analysis (with each rotation of the amplifiers). Signal intensities were kept at or near 3 V on mass 142. The long-term average reproducibility (up to and including this study) of $^{143}Nd/^{144}Nd$ on JNdi analyses on the UCSB Triton Plus was 0.512100 ± 0.000004 (2SD, N=27). Instrumental mass fractionation correction assumed an exponential fractionation law and a $^{146}Nd/^{144}Nd$ ratio of 0.7219. Sample unknowns and the BCR-2 reference material were corrected for the offset between preferred (0.512099) and measured $^{143}Nd/^{144}Nd$ on JNdi analyzed in the same barrel.

Lead isotopic compositions were measured at USC on a Thermo-Neptune MC-ICP-MS following the protocols described in Béguelin et al. (2017) and Jackson et al. (2020). Samples were corrected for instrumental fractionation using Tl addition (see White et al., 2001 for details) and assuming an exponential fractionation law. The samples, along with unleached aliquots of

278 BCR-2 processed with the sample unknowns, were corrected for offset between preferred (from
279 Eisele et al., 2003) and measured ratios of NBS981. The total procedural blanks for Sr, Nd, and
280 Pb for the samples processed at UCSB and USC are <200 pg, <50 pg, and <120 pg, respectively.
281 Four samples (ALIA-D121-09 clast [Siafiafi], RR1310-D38-08 [Waterwitch], RR1310-D31-
282 01 [Fa'aitu], and RR1310-D31-02 [Fa'aitu]) were not analyzed for Hf isotope compositions.
283

284 ## RESULTS

285 ### $^{40}Ar/^{39}Ar$ age data

286 Plagioclase separates from three samples (i.e., RR1310-D31-01 and RR1310-D31-02 from
287 Fa'aitu and RR1310-D38-08 from Waterwitch), and two groundmass samples (RR1310-D38-41
288 from Waterwitch and RR1310-D29-01 from Bustard) were targeted for $^{40}Ar/^{39}Ar$ dating (Figure
289 3). All three plagioclase separates produced sufficiently long plateaus (67–100% ^{39}Ar released),
290 probability of fit values > 5%, and $^{40}Ar/^{36}Ar$ intercept values within error of the atmospheric
291 ratio ($^{40}Ar/^{36}Ar$ = 295.5 used for standard corrections at time of analyses) (Table 2) to support a
292 robust designation for the ages. The Waterwitch plagioclase separate from sample RR1310-D38-
293 08 provided a weighted-plateau age of 10.49 ± 0.09 (2σ) Ma (Figures 1, 3). Although the

294 groundmass incremental heating results for Waterwitch sample RR1310-D38-41 provided a
295 discordant age spectrum (indicative of significant recoil effects) and was interpreted to not
296 provide an eruption age, the intermediate temperature steps are close to the 10.4-10.6 Ma
297 plagioclase age range from sample RR1310-D38-08. The two Fa'aitu plagioclase separates
298 yielded younger ages of 1.26 ± 0.14 Ma and 1.48 ± 0.19 Ma (Table 2). The Bustard groundmass
299 yielded a mini-plateau (41% ^{39}Ar released; 7 consecutive steps) age of 3.47 ± 0.02 Ma (Table 2,
300 Figure 3). We choose to include this age in our discussion as the heating spectrum plateau length
301 was reduced at either end by short bursts of excess ^{40}Ar (data points falling well outside the best
302 fit inverse isochron line and pointing toward the origin), which produced anomalously old
303 apparent ages. We recommend this sample age be treated with caution given the narrow plateau.

304 **Major element compositions**

305 The lavas in this study cover a wide range of compositions (Tables 3 and 4, Supplementary
306 Figure S1); however, all but two samples (RR1310-D31-01 and RR1310-D31-02) are alkalic.
307 The two Fa'aitu samples, RR1310-D31-01 and RR1310-D31-02, are transitional in total alkalis
308 versus SiO_2 (Macdonald and Katsura, 1964). The two Papatua glasses (PPT-D1-N1 and PPT-D1-
309 N2) and the Bustard lava (RR1310-D29-10) fall in the tephrite-basanite field, while the samples

310 from Lalla Rookh seamount (RR1310-D41-05) and Waterwitch seamount (RR1310-D38-08) fall
311 in the alkali basalt field. The most evolved lava in this study, RR1310-D39-01 from Siafiafi
312 seamount, with MgO of 0.92 wt. %, is a phonolite. Samples RR1310-D40-10, RR1310-D34-01,
313 KK8203-DR-1, KK8203-DR-9, RR1310-D29-01, and ALIA-121-09 were not analyzed for major
314 elements, due to too little sample material being available, hence a compositional designation for
315 the rock type cannot be made.
316

317 **Trace element compositions**

318 The lavas in this study exhibit a wide variety of trace element abundances (Tables 3 and 4),
319 which are displayed in primitive mantle-normalized (McDonough and Sun, 1995) trace element
320 diagrams (Supplementary Figure S2). The two Papatua glasses (PPT-D1-N1 and PPT-D1-N2)
321 are strongly enriched in incompatible trace elements and show negative K, Pb, Zr, Hf, and Ti
322 anomalies. Sample RR1310-D41-05 from Lalla Rookh shows strong incompatible trace element
323 enrichment and has slight negative Cs, Ba, U, K, and Pb anomalies. Due to limited sample size,
324 basalt clasts separated from a hyaloclastite from Lalla Rookh sample RR1310-D40-10 were not
325 analyzed for trace elements. The primitive mantle-normalized trace element pattern displayed by
326 the newly analyzed Waterwitch sample (RR1310-D38-08) has strong negative K and Pb

anomalies. The two samples from Fa'aitu (RR1310-D31-01 and RR1310-D31-02) exhibit nearly identical primitive mantle-normalized trace element patterns and are moderately enriched in incompatible trace elements, except for strong depletions in Cs and Pb and a positive Sr anomaly. Two samples from Siafiafi, RR1310-D39-01 and the basalt clast separated from hyaloclastite sample ALIA-D121-09, have dissimilar primitive mantle-normalized trace element patterns: sample RR1310-D39-01 has higher incompatible trace element concentrations than the ALIA-D121-09 clast, consistent with its highly differentiated phonolite composition, which also explains its 'spikier' pattern, with strong depletions in Ba, U, Pb, Sr, and Ti. Sample KK8203-DR-1, a basalt clast separated from a Talviuni seamount sample, has a primitive mantle-normalized trace element pattern that is broadly similar to Siafiafi sample ALIA-D121-09. Tuscarora bank sample KK8203-DR-9—the most geochemically depleted sample in this study—shows slight enrichment in several incompatible trace elements, including positive Pb, Zr, and Hf anomalies, as well as negative Ba and Sr anomalies. The Bustard seamount sample (RR1310-D29-10) shows strong incompatible trace element enrichment and a positive Sr anomaly. (Unfortunately, due to its small sample size, trace element data are not available for a second Tuscarora seamount sample (RR1310-D34-01)).

343

344 **Hafnium, Pb, Sr, and Nd isotopic compositions**

345 Based on their varied geochemical compositions, we group the lavas from this study into three
346 categories—EM1-type lavas, geochemically enriched WESAM lavas, and WESAM lavas with
347 depleted isotopic compositions—and we explore each category in detail below.

348 *EM1-type lavas*

349 The samples from Papatua seamount and Fa'aitu seamount studied here show EM1-like isotopic
350 characteristics (Figure 4). The glasses from Papatua seamount, PPT-D1-N1 and PPT-D1-N2,
351 have $^{143}Nd/^{144}Nd$ ranging from 0.512622 to 0.512631, $^{87}Sr/^{86}Sr$ of 0.705045, $^{176}Hf/^{177}Hf$ ranging
352 from 0.282877 to 0.282892, and $^{206}Pb/^{204}Pb$ ranging from 18.6861 to 18.7229. The two samples
353 from the WESAM Fa'aitu seamount, RR1310-D31-01 and RR1310-D31-02, have nearly
354 identical isotopic compositions with weak EM1-like signatures. They have $^{143}Nd/^{144}Nd$ ranging
355 from 0.512765 to 0.512771, $^{87}Sr/^{86}Sr$ ranging from 0.704586 to 0.704642, and $^{206}Pb/^{204}Pb$
356 ranging from 18.7650 and 18.7733.

357

358 *Western Samoan (WESAM) lavas with enriched isotopic compositions*

We report data from seven samples with moderately enriched geochemical compositions. Two lavas from Lalla Rookh seamount (sample RR1310-41-05 and the basaltic clasts taken from hyaloclastite sample RR1310-40-10) have isotopic signatures comparable to lavas previously dredged from Lalla Rookh seamount (Hart et al., 2004), but have slightly higher $^{87}Sr/^{86}Sr$ (up to 0.705000) and $^{143}Nd/^{144}Nd$ as low as 0.512750 (Figure 4). Siafiafi seamount lava RR1310-D39-01 shows isotopic similarities to the Lalla Rookh samples from this study and Hart et al. (2004), while the basalt clast from Siafiafi hyaloclastite sample ALIA-D121-09 has slightly more radiogenic Pb ($^{206}Pb/^{204}Pb$ of 19.7439). Additionally, basaltic clast sample ALIA-D121-09 has slightly lower $^{87}Sr/^{86}Sr$ (0.704519) than the Siafiafi seamount lava (0.705030), but similar $^{143}Nd/^{144}Nd$ (0.512775). The $^{87}Sr/^{86}Sr$ from the Siafiafi ALIA-D121-09 basaltic clast has similar $^{87}Sr/^{86}Sr$ (0.704519) to the previously published $^{87}Sr/^{86}Sr$ of a clinopyroxene megacryst separated from the same hyaloclastite sample (0.704587; see sample ALIA-D121-09 in Jackson et al., 2010). A basalt clast from Talviuni hyaloclastite sample KK8203-DR-1 has lower $^{206}Pb/^{204}Pb$ (19.0401) and $^{87}Sr/^{86}Sr$ (0.70427) than the Lalla Rookh sample RR1310-D40-10 clast, but higher $^{176}Hf/^{177}Hf$ (0.283035) and $^{143}Nd/^{144}Nd$ (0.512857). One Tuscarora bank lava, RR1310-D34-01, has even more enriched isotopic signatures than the five lavas discussed above, with $^{87}Sr/^{86}Sr$ of

375 0.707822, $^{143}Nd/^{144}Nd$ of 0.512539, $^{176}Hf/^{177}Hf$ of 0.282872, and $^{206}Pb/^{204}Pb$ of 18.7671. The
376 Waterwitch seamount lava RR1310-D38-08 has one of the most radiogenic Pb isotopic
377 compositions in this study ($^{206}Pb/^{204}Pb$ of 19.6015) (Figure 4). This Waterwitch sample has
378 slightly lower $^{143}Nd/^{144}Nd$ (0.512890) than the previous Waterwitch sample from Jackson et al.
379 (2010), but has similar $^{87}Sr/^{86}Sr$ (0.703727) and more radiogenic Pb isotopic compositions.
380
381 *Western Samoan (WESAM) lavas with depleted isotopic compositions*
382 We also report isotopic data for a Bustard seamount lava (RR1310-D29-10) and a
383 combination of basaltic clasts from a Tuscarora bank hyaloclastite (KK8203-DR-9), which
384 exhibit relatively depleted geochemical compositions. The basaltic clasts from Tuscarora bank
385 sample KK8203-DR-9 has much lower $^{87}Sr/^{86}Sr$ (0.703789) than the other Tuscarora bank lava
386 in this study (see sample RR1310-D34-01 [with $^{87}Sr/^{86}Sr = 0.707822$] above) (Figure 4).
387 Notably, the Tuscarora KK8203-DR-9 clasts show similar $^{87}Sr/^{86}Sr$, $^{143}Nd/^{144}Nd$, and $^{176}Hf/^{177}Hf$
388 but slightly more radiogenic Pb isotopes to the only other Tuscarora bank sample (RR1310-D33-
389 32; Finlayson et al., 2018), which was dredged during a different expedition (Figure 4). Bustard
390 seamount has similar Pb isotopic compositions to Tuscarora bank sample KK8203-DR-9, but

391 also has slightly higher $^{87}Sr/^{86}Sr$ (0.704102), lower $^{143}Nd/^{144}Nd$ (0.512838) and lower $^{176}Hf/^{177}Hf$

392 (0.283040).

393

394 ## DISCUSSION

395 Given that Samoan lavas exhibit such a wide variety of isotopic compositions, also we

396 explore changes in isotopic composition of lavas along the Samoan chain (Figure 5). While

397 rejuvenated lavas have lower average $^{206}Pb/^{204}Pb$, there does not appear to be any consistent

398 changes seen in $^{87}Sr/^{86}Sr$, $^{206}Pb/^{204}Pb$, or $^{143}Nd/^{144}Nd$ with longitude along the Samoan hotspot

399 track.

400 ### Tracing the "hotspot highway"

401 The "hotspot highway" consists of multiple overlapping hotspot tracks aligned on a Pacific plate

402 flow line, where the result of the overlapping hotspot tracks is a linear suite of islands and

403 seamounts that show no clear volcanic progression unless the volcanoes are separated by their

404 respective hotspots of origin (see Figure 1b and 1c). In addition to the Samoan hotspot track, the

405 hotspot highway includes the Cook-Austral Volcanic Lineament, suggested by Chauvel et al.

406 (1997) to consist of three individual age-progressive hotspot tracks: the Macdonald hotspot (also

referred to in the literature as the "Tubuai trend" and "Old Rurutu"), the Arago-Rurutu hotspot (referred to as the "Atiu trend" and "Young Rurutu"), and the Rarotonga group. This is relevant because the hotspot highway hypothesis predicts that older volcanoes associated with these three hotspots are located in the Samoan region (Jackson et al., 2010). This hypothesis successfully explains, for example, the presence of the Arago-Rurutu hotspot-related volcano Rose atoll (Figures 1, 2) near the eastern terminus of the Samoan hotspot track and likely explains the presence of two undated HIMU volcanic interlopers—Malulu seamount and the HIMU stage of Papatua seamount—in the region near the Samoan hotspot (Buff et al., 2021). In the following we explore the western (older) extents of the hotspot tracks that constitute the hotspot highway and attempt to deconvolve contributions of these hotspots to the hotspot highway with particular emphasis on determining the origin of the older HIMU stage of volcanism at Papatua.

Macdonald hotspot

Based on the Wessel and Kroenke (2008) plate motion model, the trace of the Macdonald hotspot track continues from Macdonald seamount to the Samoan region, where the hotspot trace bends north at ~50 Ma, a bend that is similar morphologically to the Hawaii-Emperor Bend

(HEB) in the region near the Samoan hotspot (Figure 1). Therefore, volcanic contributions from the Macdonald hotspot are expected 1) in the region between the Samoan hotspot and Macdonald seamount, and 2) along a trace extending to the NNW of the Samoan region into the Tokelau Islands where the Macdonald hotspot can be traced back to ~70 Ma (Koppers et al., 2007; Konter et al., 2008; Jackson et al., 2020). Critically, the plate reconstruction predicts that volcanoes related to Macdonald hotspot would not be found to the west of the main Samoan islands of the ESAM region (Figure 1 and 2). Within uncertainty of the Wessel and Kroenke (2008) plate reconstruction model, two Samoan interloper seamounts—Malulu seamount and the HIMU stage of Papatua seamount—may have been generated over the Macdonald hotspot, in which case they would have ages of ~43 to ~44 Ma. Unfortunately, samples suitable for dating have not yet been obtained from these two seamounts.

Arago-Rurutu hotspot

The Wessel and Kroenke (2008) model predicts the Arago-Rurutu hotspot track trends WNW from Arago seamount (Bonneville et al., 2006), through the region of the Samoan hotspot (Figure 1). Like the Macdonald hotspot, the Arago-Rurutu hotspot generated HIMU volcanism

(e.g. Nakamura and Tatsumoto, 1988; Chauvel et al., 1997; Hauri and Hart, 1993; Bonneville et al., 2006; Jackson et al., 2020). If the HIMU Malulu seamount or the HIMU stage of Papatua seamount formed over the Arago-Rurutu hotspot, they would have ages of ~24 to ~25 Ma.

Finlayson et al. (2018) and Konrad et al. (2018) picked up the Arago-Rurutu track at East Niulakita (42.24 ± 0.82 Ma to 45.73 ± 0.14 Ma) and Kosciusko (47.37 ± 0.11 Ma to 48.16 ± 0.19 Ma) seamounts near the predicted bend of the hotspot track (i.e., similar morphologically and chronologically to the HEB) (Figure 1). From there, the track can be traced back to >100 Ma in the Western Pacific (Koppers et al., 2003; Konter et al., 2008; Konrad et al., 2018). However, there is currently no evidence for the Arago-Rurutu hotspot track between Rose atoll (24.81 Ma; Buff et al., 2021) and East Niulakita (45.73 Ma) unless the HIMU portion of Papatua can be determined to be related to the Arago-Rurutu hotspot (Figure 1 and 2). This leaves a ~20 Ma gap in volcanism along the Arago-Rurutu hotspot track for which no record has yet been found.

Given its radiogenic Pb isotopic composition, Waterwitch seamount was a candidate interloper seamount associated with an origin over the Cook-Austral hotspots (Jackson et al., 2010). However, the robust plagioclase age for Waterwitch presented here (10.49 ± 0.09 Ma) falls on the Samoan age progression and indicates a Samoan hotspot origin. The absence of Arago-

Rurutu hotspot-derived volcanism in the region between Rose atoll and East Niulakita may relate to two mechanisms. First, Arago-Rurutu volcanoes may be buried under subsequent outpourings of lava associated with more recent passage over the Samoan hotspot (Finlayson et al., 2018). Indeed, East Niulakita hosts both older HIMU Arago-Rurutu lavas (45.73 Ma) as well as younger Samoan lavas (14.76 Ma) (Finlayson et al., 2018). Alternatively, this portion of the Arago-Rurutu hotspot track may lie further to the south than predicted by the Wessel and Kroenke (2008) model. In this case, the trace of the Arago-Rurutu hotspot would clearly intersect with the northern Tonga trench, with the result being that any Arago-Rurutu hotspot volcanoes erupted between ~25 and ~45 Ma may have been subducted into the trench. This model is consistent with the appearance of HIMU-flavored volcanoes in the northern Lau backarc basin, a possible outcome of subduction of HIMU-related Arago-Rurutu hotspot volcanoes (Price et al., 2016, 2017), but may require some modification to the plate models tested in Finlayson et al. (2018). The WNW striking portion of the Arago-Rurutu hotspot that is older than 45 Ma, and erupted prior to the Arago-Rurutu track bend, escaped subduction because it is located too far north of the northern terminus of the Tonga trench (Figure 1a); this older portion of the Arago-

Rurutu hotspot is traced through the Tuvalu and Gilbert Islands and into the Western Pacific Seamount Province (Koppers et al., 2003; Konter et al., 2008; Konrad et al., 2018).

Thus at present, the portion of the Arago-Rurutu hotspot between Aitutaki and Rose remains unsampled, and numerous seamounts between Aitutaki and Rose present targets that could potentially close this gap in the Arago-Rurutu hotspot.

Rarotonga group

Due to the lack of any known, age-progressive track linked to the active melt zone, Rarotonga is unlikely to be an authentic hotspot (Jackson et al., 2020). Instead, the entire "hotspot track" is defined by overlapping periods of volcanism at just two volcanoes spaced only ~260 km apart: Rarotonga (1.157 to 1.697 Ma) and the young stage of Aitutaki (1.382 to 1.941 Ma) (Rose and Koppers, 2019), which are located over 1200 km southwest of Papatua and have EM1 isotopic compositions. Indeed, Chauvel et al. (1997) noted that the Rarotonga hotspot is "less well expressed" than the other hotspots in the Cook-Austral Volcanic Lineament. No age-progressive volcanoes associated with this "hotspot" have been identified west of Rarotonga and Aitutaki islands. Unless Rarotonga is the product of a relatively new hotspot that only became active over the last few million years—which might explain the lack of a long-term age progression that can

be traced to the WNW of Rarotonga Island—there is no evidence of a hotspot origin for Rarotonga Island and the young stage of Aitutaki (Jackson et al., 2020). For this reason, we designate Rarotonga as a volcanic "group" rather than a hotspot track.

Samoan hotspot

The westernmost known expression of the Samoan hotspot is Alexa bank (Figures 1, 2), with an age of 23.96 Ma (Hart et al., 2004). However, the geochemistry of Alexa bank exhibits radiogenic isotopic compositions that are unusually depleted (i.e., $^{87}Sr/^{86}Sr < 0.7044$) relative to other known Samoan shield lavas (referred hereafter as Alexa-type). Finlayson et al. (2018) showed that Samoan shield lavas with depleted radiogenic isotopic signatures are not unique to Alexa bank and characterize other WESAM volcanoes along the Samoan hotspot track, including Tuscarora, Bayonnaise, and Samoan lavas from East Niulakita. The Tuscarora bank clasts and Bustard lava studied here both have compositions similar to those of the geochemically depleted Alexa-type lavas (although Bustard is slightly more geochemically enriched) (Figure 4). These lavas support the hypothesis that Samoan lavas with depleted radiogenic isotopic signatures are located widely along the WESAM region of the Samoan

503 hotspot track (a span of ~640 km from Alexa bank to Tuscarora seamount), but not in the ESAM
504 region (Figure 5): there are no volcanoes east of Savai'i with $^{87}Sr/^{86}Sr < 0.7044$, but eight
505 Samoan volcanoes with $^{87}Sr/^{86}Sr < 0.7044$ are identified west of Savai'i (nine if Nukulaelae is
506 included as a Samoan volcano; Finlayson et al., 2018). Furthermore, the basaltic clast sample
507 from Tuscarora bank (KK8203-DR-9) has much lower $^{87}Sr/^{86}Sr$ (0.703789) than the other
508 Tuscarora bank lava in this study (see sample RR1310-D34-01 [with $^{87}Sr/^{86}Sr = 0.707822$]),
509 indicating that Samoan lavas with depleted geochemistry and normal Samoan shield
510 geochemistry can be found at the same volcano.

511 Several WESAM lavas from this study (e.g. Lalla Rookh, Siafiafi, Talviuni, and the
512 Tuscarora bank lava) show moderately enriched isotopic signatures that plot close to or within
513 the range of previously published Samoan shield lavas (Figure 4). Our new geochemical and age
514 data on sample RR1310-D38-08 suggests that Waterwitch seamount, which was previously
515 grouped with non-Samoan 'interlopers' based on the radiogenic isotopic composition of one lava
516 (ALIA-D122-03; Jackson et al., 2010), is in fact Samoan. Therefore, the field for Samoan shield
517 lavas in radiogenic isotopic space should be enlarged to include Waterwitch, which has relatively

high $^{206}Pb/^{204}Pb$ (19.35 to 19.60), and plots outside the previously-known range identified for other Samoan shield volcanoes (Figure 4).

We also note that it is unlikely that the apparently older HIMU stage found at Papatua seamount was generated over the Samoan hotspot. First, the ferromanganese rind on the HIMU Papatua sample ALIA-D129-05 (>5 cm) is much thicker than the rinds, or patinas, from young Samoan volcanoes in the vicinity (< 1 mm). Second, the HIMU Pb isotopic composition ($^{206}Pb/^{204}Pb$=20.0) of the Papatua seamount lava is significantly more radiogenic than that found in Samoan lavas (Figure 4). Workman et al. (2004) suggested that the slightly more radiogenic Pb isotopes in the youngest, easternmost volcanoes along the Samoan hotspot may be a result of the Pacific plate acquiring this signature during prior passage of this region of the Pacific plate over the HIMU Cook-Austral hotspots, Arago-Rurutu and Macdonald. In this scenario, this region of Pacific lithosphere, which had previously been underplated by HIMU Cook-Austral material, rafted into the Samoan region with plate motion, which then became incorporated into the upwelling Samoan plume (or Samoan plume melts). However, the extreme HIMU signatures present in the Cook-Australs are not observed in Samoa, and Jackson et al. (2014) showed that

533 the milder HIMU signatures in some Samoan hotspot volcanoes can also be explained as being
534 part of the Samoan plume.

535

536 **Anomalously young volcanism along the Samoan hotspot track**

537 In contrast to the apparently old and visually altered Papatua sample ALIA-D129-05, the two
538 pristine Papatua glasses studied here were dredged at shallower depths (2000 mbsl) on the
539 seamount, presumably sampling stratigraphically higher, and younger, material. These Papatua
540 glass samples were attached to extremely fresh mantle xenoliths that were the subject of Poreda
541 and Farley's (1992) rare gas study. Peridotite mantle xenoliths associated with the Samoan
542 hotspot have only been reported in rejuvenated lavas (e.g. Natland, 1980; Hauri and Hart, 1994),
543 and while Poreda and Farley (1992) did not publish the major and trace element, or isotopic
544 compositions measured in the host glass, they did note that "*the chemical and Sr-Nd isotopic*
545 *compositions of the Si-undersaturated glass … leave little doubt that they were erupted by post-*
546 *erosional stage volcanics.*" The new geochemical data presented herein on these glasses support
547 Poreda and Farley's (1992) interpretation: The Papatua lavas are Si-undersaturated and plot in or
548 on the fringes of the Samoan rejuvenated field in all isotope spaces except for that of Hf-Nd (but
549 this may be due to a paucity of Hf isotope data for Samoan rejuvenated lavas) (Figure 4). We

find that the two Papatua glasses have EM1 compositions, a geochemical signature associated with rejuvenated volcanism along the nearby Samoan hotspot track, which contrasts with the HIMU compositions identified in the more deeply-dredged, ferromanganese-encrusted Papatua sample ALIA-D129-05. Both glasses appear extremely fresh, lacking visible signs of alteration or ferromanganese-encrustation. As volcanic glass and peridotite xenoliths weather rapidly in submarine conditions, the pristine nature of the Papatua glasses supports the interpretation that they are relatively young, which is inconsistent with the old age inferred for the HIMU Papatua lava (ALIA-D129-05). These differences in isotopic composition and apparent age suggest that Papatua erupted both an older HIMU stage sampled by ALIA-D129-05 and an EM1 stage inferred by Poreda and Farley (1992) to represent rejuvenated-stage volcanism. Furthermore, extreme EM1 volcanism on the nearby Uo Mamae seamount (Figures 2, 4) has been suggested to relate to Samoan rejuvenated volcanism (e.g. Regelous et al., 2008). If the Samoan rejuvenated field in radiogenic isotope space is expanded to include Samoan rejuvenated lavas *sensu stricto* as well as Uo Mamae lavas, the field encompasses Papatua rejuvenated lavas (Figure 4), suggesting a common mantle source for the EM1 Papatua and Samoan rejuvenated lavas.

565 Young, rejuvenated lavas with EM1 signatures are found capping ESAM shield volcanoes on
566 nearby Tutuila, Upolu, and Savai‘i (e.g. Hawkins and Natland, 1975; Natland and Turner, 1985;
567 Hauri and Hart, 1993; Natland, 2003; Workman et al., 2004; Konter and Jackson, 2012).
568 However, several WESAM volcanoes also appear to host anomalously young volcanism. For
569 example, Hart et al. (2004) found that a sample from Lalla Rookh seamount (located ~725 km
570 west of Vailulu‘u) erupted a much younger rejuvenated lava (1.63 ± 0.06 Ma), which falls off the
571 Samoan age progression (Figure 1b). Lavas from Wallis Island, located ~70 km southwest of
572 Lalla Rookh seamount, are also young (0.08 Ma, Price et al., 1991) and geochemically consistent
573 with rejuvenated lavas from Samoa (Price et al., 2014). Our $^{40}Ar/^{39}Ar$ ages show that one
574 Bustard lava (3.47 ± 0.02 Ma), located ~1170 km west of Vailulu‘u, as well as two Fa‘aitu
575 seamount lavas (1.26 ± 0.14 Ma and 1.48 ± 0.19 Ma) located ~1050 km west of Vailulu‘u, are
576 each ~10 million years younger than expected from a Samoan age progression (Figure 1b). The
577 two lavas from Fa‘aitu show weak EM1 signatures and plot within or close to the field for
578 Samoan rejuvenated lavas in Pb-Sr-Nd isotope space (Figure 4), so their young ages and
579 geochemistry are permissive of an origin similar to Samoan rejuvenated lavas. Unfortunately, the
580 single geochemically-characterized Bustard lava (RR1310-D29-10) does not have an available

581 age, and the 3.47 Ma Bustard lava is not geochemically characterized. The RR1310-D29-10 lava
582 has Alexa-type geochemistry that differs from most rejuvenated-stage Samoan lavas, but the
583 young age of the Bustard lava RR1310-D29-01 supports the interpretation that it represents
584 rejuvenated volcanism. However, the origin of the anomalously young volcanism in the
585 WESAM remains unclear.
586

587 **Exploring causes of rejuvenated volcanism along the Samoan hotspot track**

588 Regelous et al. (2008) argued that the extreme radiogenic isotopic compositions found at Uo
589 Mamae reflect an endmember that contributes to rejuvenated volcanism in Samoa. Hawkins and
590 Natland (1975) also noted that a young lava (0.94 Ma) dredged from the summit of Uo Mamae
591 may be rejuvenated, and Regelous et al. (2008) suggested it may have formed as the volcano
592 underwent extensional faulting while approaching the Tonga trench. In fact, it has been shown
593 that Samoan mantle material is sampled not only by Uo Mamae, but also by Tafahi and
594 Niuatoputapu, northern Tonga arc islands located, respectively, ~280 and ~300 km south of the
595 trace of the Samoan hotspot track, as well as lavas in the northern Lau basin located further to
596 the west (e.g. Wendt et al., 1997, Turner and Hawkesworth, 1998; Regelous et al., 2008; Zhang
597 et al., 2019)) (Figure 2). If Samoan-type mantle has pervaded the region beneath Papatua, which

598 is located only ~60 km south of Tutuila Island—a Samoan hotspot volcano that has erupted EM1
599 rejuvenated lavas in the past 24,000 years (Reinhard et al., 2019)—it is possible that the EM1
600 rejuvenated lavas on Papatua are also geochemically influenced by Samoan material. However,
601 while the composition of the apparently young EM1 Papatua glasses suggests a genetic link to
602 Samoan rejuvenated volcanoes—and is therefore inferred to be young—the HIMU portion of the
603 Papatua seamount ($^{206}Pb/^{204}Pb = 20.0$) is clearly not Samoan and likely relates to much older
604 volcanism associated with prior passage over one of the Cook-Austral hotspots. This raises a key
605 question: How can Samoan rejuvenated lavas manifest at a non-Samoan volcano?
606 It has been suggested that tectonic stresses produced flexural uplift in the Pacific plate near
607 the northern terminus of the Tonga trench, where the Pacific plate is tearing and the southern
608 portion is subducting (e.g. Hawkins and Natland, 1975; Natland, 1980; Levitt and Sandwell,
609 1995; Millen and Hamburger, 1998; Govers and Wortel, 2005). This uplift may trigger mantle
610 melting that taps EM1-material giving rise to rejuvenated lavas capping Samoa shield volcanoes
611 (e.g. Price et al., 1991; Hart et al., 2004; Konter and Jackson, 2012). Savai‘i, the Samoan island
612 with the most extensive rejuvenated volcanism, lies ~130 km north of the northern terminus of
613 the Tonga trench, and both the extent of rejuvenated volcanism and the proximity to the trench

614 suggest a tectonic trigger for rejuvenation (e.g. Hawkins and Natland, 1975; Koppers et al., 2008,
615 2011; Konter and Jackson, 2012).

616 Lithospheric deformation of the Pacific plate outboard of the northern Tonga Trench was
617 modeled using a 3D numerical model by Govers and Wortel (2005), which serves as the basis for
618 the "region of flexural uplift" in Figure 6. Jackson and Konter (2012) created a quantitative
619 model to show how this flexural uplift generates decompression melting that can explain
620 rejuvenated volcanism in the Samoan region. In detail, Jackson and Konter (2012) explored the
621 possible link between the timing of the onset of rejuvenated volcanism in the ESAM to a
622 volcano's approach to the trench, first on Savai'i (which is located closer to the trench) and then
623 on Tutuila (which is further from the trench). In this scenario, melting initiates during the Pacific
624 plate's approach to the trench when the plate enters a region of flexure-driven uplift at a rate of
625 ~0.4 mm/year (Figure 6; based on Govers and Wortel (2005), Konter and Jackson (2012), and
626 Reinhard et al. (2019)). To illustrate how Samoan volcanoes move into this region of high
627 flexural uplift as the Pacific plate approaches the trench, two time-steps are shown in Figure 6:
628 0.6 Ma and present day. Reinhard et al. (2019) showed that the region of high flexural uplift is
629 associated with recent rejuvenated volcanism in the Samoan region including volcanism at Uo

630 Mamae, Savai‘i, Upolu, and Tutuila. Papatua moved into this region of tectonically-induced
631 melting between 0.6 Ma and the present day. Critically, Papatua seamount is currently located
632 only ~200 km east-northeast of the northern terminus of the Tonga trench—similar to the
633 distance between Tutuila and the trench—suggesting that the same tectonic stresses that trigger
634 rejuvenated volcanism in the Samoan region might arguably also affect nearby Papatua seamount
635 (see Figure 6). Because Tutuila and Papatua would have crossed into the region of high flexural
636 uplift at a similar time, and the initiation of rejuvenated volcanism occurred at 24 ka on Tutuila
637 (Reinhard et al., 2019), tectonically-triggered rejuvenated volcanism at Papatua might also have
638 been initiated recently. In this scenario, the tectonic forces from the nearby trench triggered
639 recent rejuvenated melting of underplated Samoan mantle material that had flowed southward
640 under Papatua. The southward flow of the Samoan material toward Papatua could be facilitated
641 by the plume spreading out laterally and flattening, or “pancaking”, as it rises and impinges on
642 the base of the Pacific lithosphere (Phipps-Morgan et al., 1995), thereby explaining the presence
643 of Samoan plume material beneath a non-Samoan volcano (Papatua seamount) located ~60 km
644 south of the Samoan hotspot track (Figure 6). Thus, this simple process of tectonically-triggered
645 melting of southward advected Samoan plume material helps explain both the Samoan EM1

geochemistry and the apparent young age of the rejuvenated volcanic glasses along with older, non-Samoan HIMU lavas at Papatua seamount.

Similar to rejuvenated volcanism occurring off the axis of the Samoan hotspot at Papatua, secondary offshore volcanism at Hawai‘i has also been linked to flexural uplift (e.g. Lipman et al., 1989; Frey et al., 2000). Modeling of flexural uplift surrounding a growing volcanic shield shows this to trigger decompression of mantle plume material (Bianco et al., 2005). The material, which initially partially melted under the shield volcano, then flowed out laterally. This model is supported at Hawai‘i by the secondary volcanism at the South Arch Volcanic Field, located ~200 km south of Lō‘ihi seamount (e.g. Lipman et al., 1989). Additionally, rejuvenated lavas and ‘petit-spot’ lavas form by similar processes (lithosphere uplift and decompression), and Reinhard et al. (2019) found that petit spot volcanoes also have clear geochemical similarities (e.g. strong EM1 affinities) with Samoan rejuvenated volcanism.

In a similar vein, tectonic reactivation may also explain young volcanism in the WESAM. Utilizing a variety of geophysical data, Pelletier and Auzende (1996) determined that the WESAM region south of East Niulakita has experienced relatively recent extension and normal faulting in the region near the Vitiaz lineament. In addition to a 0.2 Ma age basalt recovered near Bayonnaise, they interpreted cone-shaped edifices as recent volcanism that was synchronous

663 with or immediately post-dating this normal faulting. Bustard (3.47 Ma) and Fa‘aitu (1.26-1.48
664 Ma) seamounts are located just south of East Niulakita in the region impacted by recent
665 extension. We therefore consider that tectonic reactivation allowed EM1 melts in the shallow
666 mantle to erupt and form the young lavas found on Bustard and Fa‘aitu, long after these
667 volcanoes passed over the Samoan hotspot. Like Fa’aitu, Wallis (0.08 Ma; Price et al., 1991) is
668 located near the Vitiaz lineament, and Lalla Rookh (1.6 Ma; Hart et al., 2004) is only 100 km
669 north of the Vitiaz lineament. If there has been wide-scale extension in the region of the Vitiaz
670 between Wallis and Fa’aitu over the past 3.5 Ma, it may explain exceptionally young volcanism
671 at all four WESAM volcanoes: Lalla Rookh, Wallis, Fa’aitu, and Bustard.
672

673 **The prospect of Cretaceous Samoan volcanism**

674 Looking beyond Alexa, it is possible that the Samoan hotspot track may extend back into the
675 Cretaceous (e.g. Koppers et al., 1998, 2003). The Wessel and Kroenke (2008) plate motion
676 model places the HEB-like bend of the Samoan chain beneath the Ontong Java Plateau, which
677 may have suppressed volcanism in the region due to its substantially increased lithospheric
678 thickness. However, 100 Ma-old seamounts located in the southern portion of the Western

679 Pacific Seamount Province, north of the Ontong Java Plateau, have ages and geochemistry
680 consistent with an origin over the Samoan hotspot (e.g. Koppers et al., 2003; Konter et al., 2008).
681 Future expeditions sampling the possible trace of the hotspot prior to 25 Ma are warranted.
682

683 ## CONCLUSIONS

684 $^{40}Ar/^{39}Ar$ data provide additional constraints on the make-up of the "hotspot highway" along the
685 Samoan hotspot track. Based on a $^{40}Ar/^{39}Ar$ age of 10.49 ± 0.09 Ma for Waterwitch, this
686 seamount falls on the Samoan age progression, consistent with a Samoan origin. This contrasts
687 with a previous suggestion that Waterwitch is a HIMU "interloper" volcano left over from
688 passage of the Pacific lithosphere over the Cook-Austral hotspots. This finding implies a paucity
689 of HIMU-interlopers west of Papatua seamount, which may be related to subduction of Cook-
690 Austral-related seamounts into the northern Tonga trench, or burial of old Cook-Austral
691 volcanoes under the lava piles of more recently-generated Samoan hotspot volcanoes.

692 It appears that Papatua seamount underwent at least two stages of volcanism, including a
693 HIMU stage (related to prior passage over either the Arago-Rurutu or Macdonald hotspots at ~25
694 or ~44 Ma, respectively), and a younger EM1 stage of rejuvenated volcanism. The EM1 Papatua

695 glasses are geochemically similar to EM1-rejuvenated lavas found in Samoa and Uo Mamae
696 seamount, which leads us to suggest that these EM1 stages at Papatua may relate to Samoan
697 rejuvenated volcanism, which is pervasive in the Samoan region. Flexural uplift in the Pacific
698 plate near the northern terminus of the Tonga trench results in melting of southward advected
699 Samoan plume material that ultimately erupts at Papatua.

700 Lastly, $^{40}Ar/^{39}Ar$ ages for Fa'aitu seamount lavas highlight the presence of exceptionally
701 young volcanism (<3.5 Ma) of unknown origin in the WESAM region. This unusual volcanism
702 may relate to regional tectonic reactivation along the Vitiaz lineament, which allowed melts in
703 the shallow mantle to erupt and form the young lavas long after the volcano passed over the
704 Samoan hotspot.

705

706 FUNDING

707 MGJ acknowledges funding from NSF grants OCE-1928970, OCE-1912931, OCE-1736984, and
708 EAR-1429648. JBT acknowledges funding from the French Agence Nationale de la Recherche
709 (grant ANR-10-BLANC-0603 M&Ms—Mantle Melting—Measurements, Models,

710 Mechanisms).

711

712 ## ACKNOWLEDGEMENTS

713 We thank Stan Hart and Hubert Staudigel for providing a sample from the 2005 Samoa ALIA
714 cruise. We also acknowledge Stan Hart for inspiring us to target the glasses on the Papatua
715 xenoliths for isotope work. We also thank Marcel Regelous and an anonymous reviewer for
716 their helpful comments. The data underlying this article are available in tables within the article.

717

718 ## REFERENCES

719

720 Adams, J. V., Jackson, M. G., Spera, F. J., Price, A. A., Byerly, B. L., Seward, G., & Cottle, J.
721 M. (2021). Extreme isotopic heterogeneity in Samoan clinopyroxenes constrains sediment
722 recycling. *Nature Communications*, *12*(1), 1-10.
723
724 Becker, J.J., Sandwell, D.T., Smith, W.H.F., Braud, J., Binder, B., Depner, J.L., Fabre, D.,
725 Factor, J., Ingalls, S., Kim, S.H. & Ladner, R. (2009). Global bathymetry and elevation data at 30
726 arc seconds resolution: SRTM30_PLUS. *Marine Geodesy*, *32*(4), 355-371.
727
728 Béguelin, P., Bizimis, M., Beier, C., & Turner, S. (2017). Rift–plume interaction reveals multiple
729 generations of recycled oceanic crust in Azores lavas. *Geochimica et Cosmochimica Acta*, *218*,
730 132-152.
731
732 Bianco, T. A., Ito, G., Becker, J. M., & Garcia, M. O. (2005). Secondary Hawaiian volcanism
733 formed by flexural arch decompression. *Geochemistry, Geophysics, Geosystems*, *6*(8).

Blichert-Toft, J., Chauvel, C., & Albarède, F. (1997). Separation of Hf and Lu for high-precision isotope analysis of rock samples by magnetic sector-multiple collector ICP-MS. *Contributions to Mineralogy and Petrology*, 127(3), 248– 260.

Blichert-Toft, J., & Albarède, F. (2009). Mixing of isotopic heterogeneities in the Mauna Kea plume conduit. *Earth and Planetary Science Letters*. 282(1), 190– 200.

Bonneville, A., Le Suavé, R., Audin, L., Clouard, V., Dosso, L., Gillot, P.Y., Janney, P., Jordahl, K. & Maamaatuaiahutapu, K. (2002). Arago Seamount: The missing hotspot found in the Austral Islands. *Geology*, 30(11), 1023– 1026.

Bonneville, A., Dosso, L. & Hildenbrand, A. (2006). Temporal evolution and geochemical variability of the South Pacific superplume activity. *Earth and Planetary Science Letters*, 244, 251– 269.

Brocher, T.M. (1985). On the age progression of the seamounts west of the Samoan islands, S.W. Pacific. *Investigations of the Northern Melanesian Borderland Circum-Pacific Council for Energy and Mineral Resources Earth Science Series*, vol. 3, pp. 173-185.

Buff, L., Jackson, M.G., Konrad, K., Konter, J. G., Bizimis, M., Price, A., Rose-Koga, E. F., Blusztajn, J., Koppers, A. A. P. & Herrera S. (2021). "Missing links" for the long-lived Macdonald and Arago hotspots, South Pacific Ocean. *Geology*, *49*(5), 541-544.

Chauvel, C., McDonough, W., Guille, G., Maury, R. & Duncan, R. (1997). Contrasting old and young volcanism in Rurutu Island, Austral chain. *Chemical Geology*. 139(1–4), 125–143.

Diraison, C. (1991). *Le volcanisme aérien des archipels polynésiens de la Société, des Marquises et des Australes-Cook. Téphrostratigraphie, datation isotopique et géochimie comparées. Contribution à l'étude des origines du volcanisme intraplaque du Pacifique Central* – Thèse de Doctorat, Univ. Bretagne Occidentale, Brest, 413 pp., dissertation.

Duncan, R. A. (1985). Radiometric ages from volcanic rocks along the New Hebrides-Samoa lineament. *Investigations of the Northern Melanesian Borderland, Circum-Pacific Council for Energy and Mineral Resources Earth Science Series*, vol. 3, Earth Science Series, pp. 67– 75.

Duncan, R. A., & McDougall, I. (1976). Linear volcanism in French Polynesia. Journal of Volcanology and Geothermal Research, 1(3), 197– 227.

Eisele, J., W. Abouchami, S. J. Galer, & Hofmann, A. W. (2003). The 320 kyr Pb isotope evolution of Mauna Kea lavas recorded in the HSDP-2 drill core. *Geochemistry, Geophysics, Geosystems*, 4(5), 8710.

Falloon, T. J., Danyushevsky, L. V., Crawford, T. J., Maas, R., Woodhead, J. D., Eggins, S. M., Bloomer, S. H., Wright, D. J., Zlobin, S. K. & Stacey, A. R. (2007). Multiple mantle plume components involved in the petrogenesis of subduction-related lavas from the northern termination of the Tonga Arc and northern Lau Basin: Evidence from the geochemistry of arc and backarc submarine volcanics. *Geochemistry, Geophysics, Geosystems*, *8*(9).

Finlayson, V. A., Konter, J. G., Konrad, K., Koppers, A. A. P., Jackson, M. G., & Rooney, T. O. (2018). Sr–Pb–Nd–Hf isotopes and 40Ar/39Ar ages reveal a Hawaii–Emperor-style bend in the Rurutu hotspot. *Earth and Planetary Science Letters*, *500*, 168-179.

Frey, F. A. (2000). Volcanism at the Edge of the Hawaiian Plume: Petrogenesis of Submarine Alkalic Lavas from the North Arch Volcanic Field. *Journal of Petrology*, 41, 667–691.

Gagnon, J. E., Fryer, B. J., Samson, I. M., & Williams-Jones, A. E. (2008). Quantitative analysis of silicate certified reference materials by LA-ICPMS with and without an internal standard. *Journal of Analytical Atomic Spectrometry. 23*(11), 1529-1537.

Gale, A., Dalton, C. A., Langmuir, C. H., Su, Y. & Schilling, J. G. (2013a). The mean composition of ocean ridge basalts. *Geochemistry, Geophysics, Geosystems*, 14, 489– 518.

797 Gale, A., Laubier, M., Escrig, S., & Langmuir, C. H. (2013b). Constraints on melting processes
798 and plume-ridge interaction from comprehensive study of the FAMOUS and North Famous
799 segments, Mid-Atlantic Ridge. *Earth and Planetary Science Letters*, *365*, 209-220.
800
801 Garçon, M., Boyet, M., Carlson, R. W., Horan, M. F., Auclair, D., & Mock, T. D. (2018).
802 Factors influencing the precision and accuracy of Nd isotope measurements by thermal
803 ionization mass spectrometry. *Chemical Geology*, *476*, 493-514.
804
805 Govers, R., & Wortel, M. J. R. (2005). Lithosphere tearing at STEP faults: Response to edges of
806 subduction zones. *Earth and Planetary Science Letters*, *236*(1-2), 505-523.
807
808 Hanyu, T., Dosso, L., Ishizuka, O., Tani, K., Hanan, B. B., Adam, C., Nakai, S. I., Senda, R.,
809 Chang, Q. & Tatsumi, Y. (2013). Geochemical diversity in submarine HIMU basalts from
810 Austral Islands, French Polynesia. *Contributions to Mineralogy and Petrology*, *166*(5), 1285-
811 1304.
812
813 Hart, S. R., Staudigel, H., Koppers, A. A., Blusztajn, J., Baker, E. T., Workman, R., Jackson, M.,
814 Hauri, E., Kurz, M., Sims, K. & Fornari, D. (2000). Vailulu'u undersea volcano: The new Samoa.
815 *Geochemistry, Geophysics, Geosystems*, 1(12), 1056.
816
817 Hart, S. R., Coetzee, M., Workman, R. K., Blusztajn, J., Johnson, K. T. M., Sinton, J. M.,
818 Steinberger, B. & Hawkins, J. W. (2004). Genesis of the Western Samoa seamount province:
819 Age, geochemical fingerprint and tectonics. *Earth and Planetary Science Letters*, 227(1), 37– 56.
820
821 Hart, S., & Blusztajn, J. (2006). Age and geochemistry of the mafic sills, ODP site 1276,
822 Newfoundland margin. *Chemical Geology*, 235, 222– 237.
823
824 Hauri, E. K., & Hart, S. R. (1993). ReOs isotope systematics of HIMU and EMII oceanic island
825 basalts from the south Pacific Ocean. *Earth and Planetary Science Letters*, 114(2), 353– 371.
826

Hauri, E. H., & Hart, S. R. (1994). Constraints on melt migration from mantle plumes: a trace element study of peridotite xenoliths from Savai'i, Western Samoa. *Journal of Geophysical Research: Solid Earth*, *99*(B12), 24301-24321.

Hawkins, J. W. & Natland, J. (1975). Nephelinites and basanites of the Samoan linear volcanic chain: Their possible tectonic significance. *Earth and Planetary Science Letters*, 24(3), 427– 439.

Jackson, M. G., Kurz, M. D., Hart, S. R., & Workman, R. K. (2007a). New Samoan lavas from Ofu Island reveal a hemispherically heterogeneous high 3He/4He mantle. *Earth and Planetary Science Letters*, *264*(3-4), 360-374.

Jackson, M. G., Hart, S. R., Koppers, A. A., Staudigel, H., Konter, J., Blusztajn, J., Kurz, M. & Russell, J. A. (2007b). The return of subducted continental crust in Samoan lavas. *Nature*, *448*(7154), 684-687.

Jackson, M. G., Hart, S. R., Konter, J. G., Koppers, A. A., Staudigel, H., Kurz, M. D., Blusztajn, J. & Sinton, J. M. (2010). Samoan hot spot track on a "hot spot highway": Implications for mantle plumes and a deep Samoan mantle source. *Geochemistry, Geophysics, Geosystems*, 11, Q12009.

Jackson, M. G., Hart, S. R., Konter, J. G., Kurz, M. D., Blusztajn, J., & Farley, K. A. (2014). Helium and lead isotopes reveal the geochemical geometry of the Samoan plume. *Nature*, 514, 355– 358.

Jackson, M. G., Koga, K. T., Price, A., Konter, J. G., Koppers, A. A., Finlayson, V. A., Konrad, K., Hauri, E. H., Kylander-Clark, A., Kelley, K. A. & Kendrick, M. A. (2015). Deeply dredged submarine HIMU glasses from the Tuvalu Islands, Polynesia: Implications for volatile budgets of recycled oceanic crust. *Geochemistry, Geophysics, Geosystems*, *16*(9), 3210-3234.

Jackson, M. G., Price, A. A., Blichert-Toft, J., Kurz, M. D., & Reinhard, A. A. (2017). Geochemistry of lavas from the Caroline hotspot, Micronesia: Evidence for primitive and

recycled components in the mantle sources of lavas with moderately elevated 3He/4He. *Chemical Geology*, *455*, 385-400.

Jackson, M. G., Halldórsson, S. A., Price, A., Kurz, M. D., Konter, J. G., Koppers, A. A. P., & Day, J. M. D. (2020). Contrasting Old and Young Volcanism from Aitutaki, Cook Islands: Implications for the Origins of the Cook–Austral Volcanic Chain. *Journal of Petrology*, *61*(3), egaa037.

Jochum, K.P., Weis, U., Schwager, B., Stoll, B., Wilson, S.A., Haug, G.H., Andreae, M.O. & Enzweiler, J. (2016). Reference values following ISO guidelines for frequently requested rock reference materials. *Geostandards and Geoanalytical Research*, *40*(3), 333-350.

Jochum, K.P., Stoll, B., Herwig, K., Willbold, M., Hofmann, A.W., Amini, M., Aarburg, S., Abouchami, W., Hellebrand, E., Mocek, B. & Raczek, I. (2006). MPI-DING reference glasses for in situ microanalysis: New reference values for element concentrations and isotope ratios. *Geochemistry, Geophysics, Geosystems*, *7*(2).

Johnson, K.T.M., Sinton, J. M., & Price, R. C. (1986). Petrology of seamounts northwest of Samoa and their relation to Samoan volcanism. *Bulletin of volcanology*, 48, 225 – 235.

Johnson, K. T. M., & Sinton, J. M. (1990). Petrology, Tectonic Setting, and the Formation of Back-arc Basin Basalts in the North Fiji Basin. *Geologisches Jahrbuch Reihe D Heft*, 92, 517–545.

Knaack, C., Cornelius, S., & Hooper, P. R. (1994). Trace element analyses of rocks and minerals by ICP-MS. *Open File Report*, Department of Geology, Washington State University, Pullman, Washington.

Konrad, K., Koppers, A. A., Steinberger, B., Finlayson, V. A., Konter, J. G., & Jackson, M. G. (2018). On the relative motions of long-lived Pacific mantle plumes. *Nature Communications*, *9*(1), 1-8.

890 Konter, J. G., Hanan, B. B., Blichert-Toft, J., Koppers, A. A., Plank, T., & Staudigel, H. (2008).
891 One hundred million years of mantle geochemical history suggest the retiring of mantle plumes
892 is premature. *Earth and Planetary Science Letters*, *275*(3-4), 285-295.
893
894 Konter, J. G., & Jackson, M. G. (2012). Large volumes of rejuvenated volcanism in Samoa:
895 Evidence supporting a tectonic influence on late-stage volcanism. *Geochemistry, Geophysics,*
896 *Geosystems*, 13, Q0AM04.
897
898 Konter, J. G., & Storm, L. P. (2014). High precision 87Sr/86Sr measurements by MC-ICP-MS,
899 simultaneously solving for Kr interferences and mass-based fractionation. *Chemical*
900 *Geology*, *385*, 26-34.
901
902 Koppers, A. A. (2002). ArArCALC—software for 40Ar/39Ar age calculations. *Computers &*
903 *Geosciences*, *28*(5), 605-619.
904
905 Koppers, A. A., Staudigel, H., Pringle, M. S. & Wijbrans, J. R. (2003). Short-lived and
906 discontinuous intraplate volcanism in the South Pacific: Hot spots or extensional volcanism?
907 *Geochemistry, Geophysics, Geosystems,* 4(10), 1089.
908
909 Koppers, A. A., Staudigel, H., Wijbrans, J. R., & Pringle, M. S. (1998). The Magellan seamount
910 trail: implications for Cretaceous hotspot volcanism and absolute Pacific plate motion. *Earth and*
911 *Planetary Science Letters*, *163*(1-4), 53-68.
912
913 Koppers, A. A., Staudigel, H., Phipps Morgan, J., & Duncan, R. A. (2007). Nonlinear 40Ar/39Ar
914 age systematics along the Gilbert Ridge and Tokelau Seamount Trail and the timing of the
915 Hawaii-Emperor Bend. *Geochemistry, Geophysics, Geosystems*, *8*(6).
916
917 Koppers, A. A., Russell, J. A., Jackson, M. G., Konter, J., Staudigel, H. & Hart, S. R. (2008).
918 Samoa reinstated as a primary hotspot trail. *Geology*, 36(6), 435– 438.
919

Koppers, A. A., Russell, J. A., Roberts, J., Jackson, M. G., Konter, J. G., Wright, D. J., Staudigel, H. & Hart, S. R. (2011). Age systematics of two young en echelon Samoan volcanic trails. *Geochemistry, Geophysics, Geosystems,* 12, Q07025.

Kuiper, K. F., Deino, A., Hilgen, F. J., Krijgsman, W., Renne, P. R., & Wijbrans, A. J. (2008). Synchronizing rock clocks of Earth history. *Science*, *320*(5875), 500-504.

Le Bas, M. J., Maitre, R.L., Streckeisen, A., & Zanettin, B. (1986). A chemical classification of volcanic rocks based on the total alkali-silica diagram. *Journal of Petrology*, 27(3), 745– 750.

Levitt, D. A., & Sandwell, D. T. (1995). Lithospheric bending at subduction zones based on depth soundings and satellite gravity. *Journal of Geophysical Research: Solid Earth*, *100*(B1), 379-400.

Lipman, P. W., Clague, D. A., Moore, J. G., & Holcomb, R. T. (1989). South Arch volcanic field—Newly identified young lava flows on the sea floor south of the Hawaiian Ridge. *Geology*, *17*(7), 611-614.

Matsuda, J. I., Notsu, K., Okano, J., Yaskawa, K., & Chungue, L. (1984). Geochemical implications from Sr isotopes and K-Ar age determinations for the Cook-Austral Islands chain. *Tectonophysics*, *104*(1-2), 145-154.

MacDonald, G. A., & Katsura, T. (1964). Chemical composition of Hawaiian lavas. *Journal of Petrology*, *5*(1), 82-133.

Maury, R. C., Guille, G., Guillou, H., Chauvel, C., Rossi, P., Pallares, C., & Legendre, C. (2013). Temporal evolution of a Polynesian hotspot: New evidence from Raivavae (Austral islands, South Pacific ocean). *Bulletin de la Société géologique de France*, *184*(6), 557-567.

McDonough, W. F., & Sun, S. S. (1995). The composition of the Earth. *Chemical Geology*, *120*(3-4), 223-253.

McDougal, I. (2010). Age of volcanism and its migration in the Samoa Islands. *Geological Magazine*, *147*(5), 705-717.

McNutt, M. K., Caress, D. W., Reynolds, J., Jordahl, K. A., & Duncan, R. A. (1997). Failure of plume theory to explain midplate volcanism in the southern Austral islands. *Nature*, *389*(6650), 479-482.

Melson, W. G., O'Hearn, T. & Jarosewich, E. (2002). A data brief on the Smithsonian Abyssal Volcanic Glass Data File,. *Geochemistry, Geophysics, Geosystems*, 3(4), 1023.

Millen, D. W., & Hamburger, M. W. (1998). Seismological evidence for tearing of the Pacific plate at the northern termination of the Tonga subduction zone. *Geology*, *26*(7), 659-662.

Min, K., Mundil, R., Renne, P. R., & Ludwig, K. R. (2000). A test for systematic errors in 40Ar/39Ar geochronology through comparison with U/Pb analysis of a 1.1-Ga rhyolite. *Geochimica et Cosmochimica Acta*, *64*(1), 73-98.

Morgan, W. J. (1971). Convection plumes in the lower mantle. *Nature*, *230*(5288), 42-43.

Morgan, W. J. (1972). Deep mantle convection plumes and plate motions. *AAPG bulletin*, *56*(2), 203-213.

Nakamura, Y., & Tatsumoto, M. (1988). Pb, Nd, and Sr isotopic evidence for a multicomponent source for rocks of Cook-Austral Islands and heterogeneities of mantle plumes. *Geochimica et Cosmochimica Acta*, *52*(12), 2909-2924.

Natland, J. H. (2003), *The Samoan Chain: A Shallow Lithospheric Fracture System*. [Available at http://www.mantleplumes.org/Samoa.html.]

Natland, J. H., & Turner, D. L. (1985). Age progression and petrological development of Samoan shield volcanoes: Evidence from K-Ar ages, lava compositions, and mineral studies.

Investigations of the Northern Melanesian Borderland, Circum-Pacific Council for Energy and Mineral Resources Earth Science Series, vol. 3, pp. 139–171.

Natland, J. H. (1980). The progression of volcanism in the Samoan linear volcanic chain. *American Journal of Science, 280*, 709-735.

Oulton, J., Humayun, M., Fedkin, A., & Grossman, L. (2016). Chemical evidence for differentiation, evaporation and recondensation from silicate clasts in Gujba. *Geochimica et Cosmochimica Acta*, *177*, 254-274.

Pearce, J. A., Kempton, P. D., & Gill, J. B. (2007). Hf–Nd evidence for the origin and distribution of mantle domains in the SW Pacific. *Earth and Planetary Science Letters*, *260*(1-2), 98-114.

Pelletier, B., & Auzende, J. M. (1996). Geometry and structure of the Vitiaz trench lineament (SW Pacific). *Marine Geophysical Researches*, *18*(2), 305-335.

Phipps Morgan, J., Morgan, W. J., Zhang, Y. S., & Smith, W. H. (1995). Observational hints for a plume-fed, suboceanic asthenosphere and its role in mantle convection. *Journal of Geophysical Research: Solid Earth*, *100*(B7), 12753-12767.

Poreda, R. J., & Farley, K. A. (1992). Rare gases in Samoan xenoliths. *Earth and Planetary Science Letters*, *113*(1-2), 129-144.

Price, R. C., Maillet, P., McDougall, I. & Dupont, J. (1991). The geochemistry of basalts from the Wallis Islands, northern Melanesian Borderland: Evidence for a lithospheric origin for Samoan-type basaltic magmas? *Journal of Volcanology and Geothermal Research,* 45(3), 267–288.

Price, A. A., Jackson, M. G., Blichert-Toft, J., Hall, P. S., Sinton, J. M., Kurz, M. D. & Blusztajn, J. (2014). Evidence for a broadly distributed Samoan-plume signature in the northern Lau and North Fiji Basins. *Geochemistry, Geophysics, Geosystems*, 15, 986– 1008.

Price, A.A., Jackson, M.G., Blichert-Toft, J., Blusztajn, J., Conatser, C.S., Konter, J.G., Koppers, A.A. & Kurz, M.D. (2016). Geochemical evidence in the northeast Lau Basin for subduction of the Cook-Austral volcanic chain in the Tonga Trench. *Geochemistry, Geophysics, Geosystems*, 17, 1694– 1724.

Price, A. A., Jackson, M. G., Blichert-Toft, J., Kurz, M. D., Gill, J., Blusztajn, J., Jenner, F., Brens, R. & Arculus, R. (2017). Geodynamic implications for zonal and meridional isotopic patterns across the northern Lau and North Fiji Basins. *Geochemistry, Geophysics, Geosystems*, *18*(3), 1013-1042.

Regelous, M., Turner, S., Falloon, T. J., Taylor, P., Gamble, J., & Green, T. (2008). Mantle dynamics and mantle melting beneath Niuafo'ou Island and the northern Lau back-arc basin. *Contributions to Mineralogy and Petrology*, *156*(1), 103-118.

Reinhard, A. A., Jackson, M. G., Koornneef, J. M., Rose-Koga, E. F., Blusztajn, J., Konter, J. G., Koga, K. T., Wallace, P. J. & Harvey, J. (2018). Sr and Nd isotopic compositions of individual olivine-hosted melt inclusions from Hawai'i and Samoa: Implications for the origin of isotopic heterogeneity in melt inclusions from OIB lavas. *Chemical Geology*, *495*, 36-49.

Reinhard, A. A., Jackson, M. G., Blusztajn, J., Koppers, A. A., Simms, A. R., & Konter, J. G. (2019). "Petit Spot" Rejuvenated Volcanism Superimposed on Plume-Derived Samoan Shield Volcanoes: Evidence From a 645-m Drill Core From Tutuila Island, American Samoa. *Geochemistry, Geophysics, Geosystems*, *20*(3), 1485-1507.

Rose, J., & Koppers, A. A. (2019). Simplifying Age Progressions within the Cook-Austral Islands using ARGUS-VI High-Resolution 40Ar/39Ar Incremental Heating Ages. *Geochemistry, Geophysics, Geosystems*, *20*(11), 4756-4778.

Ruellan, E., Delteil, J., Wright, I., & Matsumoto, T. (2003). From rifting to active spreading in the Lau Basin–Havre Trough backarc system (SW Pacific): Locking/unlocking induced by seamount chain subduction. *Geochemistry, Geophysics, Geosystems*, *4*(5).

Salters, V. J., Mallick, S., Hart, S. R., Langmuir, C. E., & Stracke, A. (2011). Domains of depleted mantle: New evidence from hafnium and neodymium isotopes. *Geochemistry, Geophysics, Geosystems*, *12*(8).

Sinton, J. M., Johnson, K. T. M., & Price, R.C. (1985). Petrology and geochemistry of volcanic rocks from the Northern Melanesian Borderland. Investigations of the Northern Melanesian Borderland, *Circum-Pacific Council for Energy and Mineral Resources Earth Science Series*, vol. 3, pp. 35 – 65.

Staudigel, H., Hart, S. R., Koppers, A. A., Constable, C., Workman, R., Kurz, M., & Baker, E. T. (2004). Hydrothermal venting at Vailulu'u Seamount: The smoking end of the Samoan chain. *Geochemistry, Geophysics, Geosystems*, *5*(2).

Staudigel, H., Hart, S.R., Pile, A., Bailey, B.E., Baker, E.T., Brooke, S., Connelly, D.P., Haucke, L., German, C.R., Hudson, I. & Jones, D. (2006). Vailulu'u Seamount, Samoa: Life and death on an active submarine volcano. *Proceedings of the National Academy of Sciences*, *103*(17), 6448-6453.

Tanaka, T., Togashi, S., Kamioka, H., Amakawa, H., Kagami, H., Hamamoto, T., Yuhara, M., Orihashi, Y., Yoneda, S., Shimizu, H. & Kunimaru, T. (2000). JNdi-1: a neodymium isotopic reference in consistency with LaJolla neodymium. *Chemical Geology*, *168*(3-4), 279-281.

Turner, D. L., & Jarrard, R. D. (1982). K-Ar dating of the Cook-Austral island chain: A test of the hot-spot hypothesis. *Journal of Volcanology and Geothermal Research*, *12*(3-4), 187-220.

Turner, S., & Hawkesworth, C. (1998). Using geochemistry to map mantle flow beneath the Lau Basin. *Geology*, *26*(11), 1019-1022.

Weis, D., Kieffer, B., Maerschalk, C., Barling, J., De Jong, J., Williams, G.A., Hanano, D., Pretorius, W., Mattielli, N., Scoates, J.S. & Goolaerts, A. (2006). High-precision isotopic

characterization of USGS reference materials by TIMS and MC-ICP-MS. *Geochemistry, Geophysics, Geosystems*, *7*(8).

Wendt, J. I., Regelous, M., Collerson, K. T., & Ewart, A. (1997). Evidence for a contribution from two mantle plumes to island-arc lavas from northern Tonga. *Geology*, *25*(7), 611-614.

Wessel, P., & Kroenke, L. W. (2008). Pacific absolute plate motion since 145 Ma: An assessment of the fixed hot spot hypothesis, *Journal of Geophysical Research*, 113, B06101.

White, W. M., Albarède, F., & Télouk, P. (2000). High-precision analysis of Pb isotope ratios by multi-collector ICP-MS. *Chemical Geology*, *167*(3-4), 257-270.

Workman, R.K., Hart, S.R., Jackson, M., Regelous, M., Farley, K.A., Blusztajn, J., Kurz, M. & Staudigel, H. (2004). Recycled metasomatized lithosphere as the origin of the Enriched Mantle II (EM2) end-member: Evidence from the Samoan Volcanic Chain. *Geochemistry, Geophysics, Geosystems*, 5, Q04008.

Workman, R. K., & Hart, S. R. (2005). Major and trace element composition of the depleted MORB mantle (DMM). *Earth and Planetary Science Letters*, *231*(1-2), 53-72.

Woodhead, J. D., & Hergt, J. M. (2000). Pb-isotope analyses of USGS reference materials. *Geostandards Newsletter*, *24*(1), 33-38.

Wright, E., & White, W. M. (1987). The origin of Samoa: new evidence from Sr, Nd, and Pb isotopes. *Earth and Planetary Science Letters*, *81*(2-3), 151-162.

Zhang, H., Yan, Q., Li, C., Zhu, Z., Zhao, R., & Shi, X. (2019). Geochemistry of diverse lava types from the Lau Basin (South West Pacific): Implications for complex back-arc mantle dynamics. *Geological Journal*, *54*(6), 3643-3659.

1110

1111 FIGURE CAPTIONS

1112 **Figure 1.** Hotspot reconstruction, age progression, and cross section. Panel (a) shows the Samoan
1113 trend and the Cook-Austral hotspot tracks (Macdonald, Arago-Rurutu, and Rarotonga) consistent
1114 with the Wessel and Kroenke (2008) absolute plate motion model. The locations of the active
1115 hotspots are marked with stars. The location of the Rarotonga hotspot, if it exists, remains to be
1116 discovered and is shown as a star with a question mark. Panel (b) shows the age progression for
1117 the Macdonald, Arago-Rurutu, Rarotonga, and Samoa hotspot tracks based on Wessel and
1118 Kroenke (2008) (WK08 APM); ages for the Cook-Austral volcanoes are summarized in Jackson
1119 et al. (2020) and Buff et al. (2021), while Samoan ages are summarized in Koppers et al. (2008).
1120 New ages for Waterwitch, Fa‘aitu, and Bustard seamounts are also shown: Waterwitch clearly
1121 lies on the Samoan hotspot age progression, and Fa‘aitu and Bustard do not (but could represent
1122 rejuvenated volcanism). Panel (c) shows a cartoon cross section that links volcanoes from the
1123 age-distance plot (panel b) to their respective hotspot (note color coding in both panels).
1124 Volcanoes with two known stages of volcanism (e.g. Rurutu, Arago, Aitutaki, Papatua, and East
1125 Niulakita) are represented by two colors on a single volcano with the bottom color relating to the

first stage of volcanism and the top color relating to the second stage. The older stage of Papatua is shown in a medium grey as we are currently unable to determine if this HIMU stage is related to the Macdonald hotspot or the Arago-Rurutu hotspot. Location of the sampled region in Figure 2 is shown in panel (a). The equivalent HEB (Hawaii-Emperor Bend) locations for the Macdonald and Arago-Rurutu hotspots are marked on the map (a) and age-distance figure (b).

Figure 2. Map of the study region including sample locations and other important volcanoes and geologic features. Volcanoes characterized in this study, and important volcanoes mentioned in the text, are marked with symbols, which are used in successive figures. Ages below each volcano are in millions of years and represent the youngest and oldest lavas from that volcano. Volcanoes with only one dated lava have a single age, while volcanoes marked with "no age" have no published age. Ages are from this study, Hawkins and Natland (1975), Price et al. (1991), Hart et al. (2004), Koppers et al. (2008, 2011), McDougall (2010), Finlayson et al. (2018), Konrad et al. (2018), and Buff et al. (2021). Base map was created using GeoMapApp (http://www.geomapapp.org) with topographic and bathymetric data from SRTM_PLUS (Becker et al., 2009). WESAM (western Samoa) and ESAM (eastern Samoa) regions are shown.

1142

1143 **Figure 3.** $^{40}Ar/^{39}Ar$ age determination results. Incremental heating (left) and inverse isochron

1144 (right) $^{40}Ar/^{39}Ar$ analyses for Fa'aitu, Bustard, ad Waterwitch seamounts. The portion of the

1145 plateaus used in the age calculations are indicated with grey lines. Filled squares in the inverse

1146 isochrons represent steps used in the plateau age calculation. Dashed lines represent the best fit

1147 isochrons with the corresponding initial $^{40}Ar/^{36}Ar$ values shown. Uncertainties are shown with

1148 2σ confidence. Data are listed in Table 2.

1149

1150 **Figure 4.** Strontium, Nd, Hf, and Pb isotopic variations for lavas in this study. The data are

1151 divided into the following fields: Samoan shield, Samoan rejuvenated, Alexa-type Samoa

1152 (depleted Samoan shield), Arago-Rurutu hotspot, Rarotonga group, and Macdonald hotspot. For

1153 the following seamounts, previously published data are distinguished from data of this study by

1154 smaller symbol size, and include data from Waterwitch seamount (Jackson et al., 2010), Lalla

1155 Rookh seamount (Hart et al., 2004), and Tuscarora seamount (Finlayson et al., 2018).

1156 Additionally, previously published data on lavas from the older series of Papatua (Jackson et al.,

1157 2010), Uo Mamae (Pearce et al., 2007; Regelous et al., 2008), Malulu seamount, Rose atoll,

Moki seamount (Jackson et al., 2010 and Buff et al., 2021), as well as older Arago-Rurutu hotspot-sourced and younger Samoa hotspot-sourced lavas from East Niulakita (Finlayson et al., 2018) are also shown with separate symbols. A dashed line extends to connect the Samoan rejuvenated field to Uo Mamae (which is likely genetically related to Samoan rejuvenated lavas; Regelous et al., 2008) and encompasses the Papatua seamount glasses. The Samoa shield field comprises data for ESAM shield lavas, while the Samoa rejuvenated field comprises data for ESAM rejuvenated lavas and lavas from Wallis Island. Data forming the Samoan fields are from the following studies: Wright and White (1987), Workman et al. (2004), Workman and Hart (2005), Jackson et al. (2007a, 2007b, 2010), Salters et al. (2011), Price et al. (2014), and Finlayson et al. (2018). The Macdonald, Arago-Rurutu (the <10 Ma Cook-Austral data plus East Niulakita only), and Rarotonga data fields are from Jackson et al. (2020).

Figure 5. The $^{87}Sr/^{86}Sr$, $^{143}Nd/^{144}Nd$, and $^{206}Pb/^{204}Pb$ versus longitude of Samoan volcanoes; data for Samoan shield stage and rejuvenated lavas are shown separately. Only the young stages of Papatua and East Niulakita are shown. The non-Samoan interlopers (Rose atoll, Malulu, the older HIMU stage of Papatua, Moki, and the older stage at East Niulakita) are not shown.

1174 Samples with red outlines are from this study. The determination of rejuvenated volcanism on
1175 the subaerial volcanoes is based on field relationships, but rejuvenated volcanism at submarine
1176 locations is based on previously published work that includes a combination of ages and isotopic
1177 composition. For example, Hart et al. (2004) suggested samples 3-26 from Lalla Rookh and
1178 ANT 239-1 from Pasco were rejuvenated based on ages and chemistry. The longitude of each
1179 volcano is chosen to be a single value for simplicity. Lead isotope data include only those
1180 collected by MC-ICP-MS.
1181
1182 **Figure 6.** Regional tectonic model for rejuvenated volcanism. Maps show the evolution of the
1183 Samoan hotspot region at 0.6 Ma and the present day. The plate reconstruction is based on
1184 Koppers et al. (2008), Ruellan et al. (2003), and Hart et al. (2004). The yellow shaded area
1185 shows the region where upward plate velocity is >0.4 mm/year, and is based on the finite
1186 difference model of Govers and Wortel (2005) and follows Konter and Jackson (2012).
1187 Volcanoes with a known Samoan origin have grey 'bases'. The 'base' of Papatua seamount,
1188 which may originate from either of the two upstream HIMU hotspots—Arago-Rurutu or
1189 Macdonald (but not Samoa)—is green. Volcanoes with yellow-colored 'tops' indicate the

1190 presence of Samoan EM1 rejuvenated lavas on that volcano (including Lalla Rookh, Pasco, and
1191 Wallis, which have ages and/or geochemical signatures which support a rejuvenated stage). Dead
1192 fish, from the inspirational figure of Natland (1980), marks the westward subduction of the
1193 Pacific plate. The Tonga trench has moved to the east over the past 0.6 Ma, while the Samoan
1194 volcanoes have moved westward on the Pacific plate. In our cartoon, Ta'u island, which was
1195 active from 0.02-0.7 Ma, is located atop the Samoan plume at the 0.6 Ma time step.
1196
1197
1198
1199
1200
1201
1202

Table 1. Sample Descriptions[1]

Sample Name	Location	Lat	Lon	WESAM or ESAM	Rock description	Prev. publ. isotopic data from same volcano?	Isotopic data in this study	Major element data in this study	Trace element data in this study	$^{40}Ar/^{39}Ar$ age in this study
PPT-D1-N1 glass	Papatua	-14.77	-170.67	ESAM	Fresh pillow glass attached to peridotite xenolith	Yes; Jackson et al., 2010 (ALIA-DR129-05); xenoliths analyzed by Poreda and Farley, 1992	Yes	Yes	Yes	No
PPT-D1-N2 glass	Papatua	-14.77	-170.67	ESAM	Fresh pillow glass attached to peridotite xenolith	Yes; Jackson et al., 2010 (ALIA-DR129-05); xenoliths analyzed by Poreda and Farley, 1992	Yes	Yes	Yes	No
RR1310-D41-05	Lalla Rookh	-12.92	-175.39	WESAM	Fresh aphanitic basalt	Yes; Hart et al., 2004 (KK820316 3-26, 3-36, and 3-43)	Yes	Yes	Yes	No
RR1310-D40-10 clast	Lalla Rookh	-12.65	-175.41	WESAM	Four ~2 cm clasts of visually altered basaltic material separated from hyaloclastite; clasts were visually similar lithology, and were combined for analysis	Yes; Hart et al., 2004 (KK820316 3-26, 3-36, and 3-43)	Yes	No	No	No

RR1310-D39-01	Siafiafi	-12.30	-176.06	WESAM	Fresh aphanitic basalt	Yes; clinopyroxene separate from Jackson et al., 2010 (ALIA-DR121-09)	Yes	Yes	Yes	No
ALIA-D121-09 clast	Siafiafi	-12.33	-175.75	WESAM	Visually altered basaltic clast picked from hyaloclastite	Yes; clinopyroxene separate from Jackson et al., 2010 (ALIA-DR121-09)	Yes	No	Yes	No
RR1310-D29-01	Bustard	-11.52	-179.70	WESAM	Fresh alkali basalt	No	No	No	No	Yes
RR1310-D29-10	Bustard	-11.52	-179.70	WESAM	Fresh vesicular pillow basalt	No	Yes	Yes	Yes	No
RR1310-D34-01	Tuscarora	-11.98	-178.27	WESAM	A small (~3 cm) piece of fresh basaltic spatter	Yes; Finlayson et al., 2018 (RR1310-D33-32)	Yes	No	No	No
KK8203-DR-9 clast	Tuscarora	-11.85	-177.88	WESAM	Multiple small (<1 cm), lithologically similar clasts of basalt picked from hyaloclastite; the clasts were visually similar in lithology, and were combined for analysis due to limited material	Yes; Finlayson et al., 2018 (RR1310-D33-32)	Yes	No	Yes	No
RR1310-D38-08	Waterwitch	-12.78	-176.50	WESAM	Lightly altered basalt	Yes; Jackson et al., 2010 (ALIA-DR122-03)	Yes	Yes	Yes	Yes
KK8203-DR-1 clast	Talviuni	-12.27	-174.63	WESAM	Visually altered vesicular basaltic clast picked from hyaloclastite	No	Yes	No	Yes	No

RR1310-D31-01	Fa'aitu	-12.79	-178.88	WESAM	Fresh plagioclase ultraphyric basalt	No	Yes	Yes	Yes	Yes
RR1310-D31-02	Fa'aitu	-12.79	-178.88	WESAM	Fresh plagioclase ultraphyric basalt	No	Yes	Yes	Yes	Yes

1. The amount of material limited the types of analyses that were carried out for some of the samples in this study. Isotopic, major and trace element data are available only for the largest samples. Samples with only isotopic and trace element data are from smaller samples. The smallest samples only have isotopic data. Due to visible alteration for some of the samples in this study, an intensive leaching procedure was applied to all but two samples prior to dissolution and chemistry; the Papatua glasses were subjected to less intensive leaching.

Table 2. $^{40}Ar/^{39}Ar$ Ages

Sample Information			Plateau										Inverse Isochron					
Sample Name	Material	Seamount	**Age**	**± 2S (i)**	± 2S (f)	^{39}Ar	K/Ca	± 2S	MSWD	P	n	N	**Age**	**± 2S (i)**	± 2S (f)	$^{40}Ar/^{36}Ar$ intercept	± 2S	SF
RR1310-D29-01*	Groundmass	Bustard	**3.47**	**±0.02 Ma**	± 0.08 Ma	41%	0.124	±0.003	0.86	53%	7	31	3.49	±0.09 Ma	± 0.12 Ma	273.14	±129.73	3%
RR1310-D31-01	Plagioclase	Fa'atiu	**1.26**	**±0.14 Ma**	± 0.14 Ma	100%	0.005	±0.000	0.73	81%	22	24	1.26	±0.16 Ma	± 0.16 Ma	290.88	±9.81	50%
RR1310-D31-02	Plagioclase	Fa'atiu	**1.48**	**±0.19 Ma**	± 0.19 Ma	90%	0.005	±0.000	0.49	97%	20	24	1.51	±0.21 Ma	± 0.21 Ma	289.34	±21.82	58%
RR1310-D38-08	Plagioclase	Waterwitch	**10.49**	**±0.09 Ma**	± 0.25 Ma	67%	0.014	±0.000	0.62	84%	14	21	10.49	±0.24 Ma	± 0.34 Ma	298.56	±31.34	16%
RR1310-D38-41	Plagioclase	Waterwitch	**N/A**															

Summary of $^{40}Ar/^{39}Ar$ age analysis on five groundmass and/or plagioclases from dredges RR1310-D29, RR1310-D31 and RR1310-D38. i=internal uncertainty; f=full uncertainty; MSWD=Mean square of weighted deviations; P = probability of fit; n=steps used in age calculation; N=total steps; SF = spreading factor; *indicates the age is a mini plateau and should be interpreted with caution.

Table 3. Major and trace element analyses of lavas examined in this study.

Sample Name		RR1310-D29-10	RR1310-D31-01	RR1310-D31-02	RR1310-D38-08	RR1310-D39-01	RR1310-D41-05	KK8203-DR-1	KK8203-DR-9	ALIA-D121-09	BCR-2	Preferred BCR-2 (Jochum et al., 2016)
Volcano		Bustard	Fa'aitu	Fa'aitu	Waterwitch	Siafiafi	Lalla Rookh	Talviuni	Tuscarora	Siafiafi		
Material analyzed		Whole rock powder	Whole rock powder	Whole rock powder	Whole rock powder	Whole rock powder	Whole rock powder	Whole rock powder	Whole rock powder	Whole rock powder	Whole rock powder	-
Method of Major Element Analysis		XRF[1]	XRF[1]	XRF[1]	XRF[1]	XRF[1]	XRF[1]	-	-	-	XRF[1]	-
Method of Trace Element Analysis		XRF, solution ICP[2]	XRF, solution ICP[2]	XRF, solution ICP[2]	XRF, solution ICP[2]	XRF, solution ICP[2]	XRF, solution ICP[2]	Solution ICP[2]	Solution ICP[2]	Solution ICP[2]	Solution ICP[2]	-
XRF Majors												
SiO_2	(wt. %)	45.3	50.0	50.2	47.3	57.1	45.3	-	-	-	54.3	54.9
TiO_2	(wt. %)	2.5	1.9	1.9	4.0	0.3	2.7	-	-	-	2.3	2.3
Al_2O_3	(wt. %)	15.3	17.2	16.9	13.7	18.8	9.9	-	-	-	13.5	13.7
FeO_{tot}	(wt. %)	8.4	9.4	9.3	12.8	2.5	11.4	-	-	-	12.5	12.6
MnO	(wt. %)	0.2	0.1	0.1	0.2	0.2	0.2	-	-	-	0.2	0.2
MgO	(wt. %)	9.0	5.2	5.7	5.9	0.9	13.1	-	-	-	3.6	3.7
CaO	(wt. %)	9.1	11.1	10.9	10.7	1.2	10.2	-	-	-	7.1	7.2
Na_2O	(wt. %)	4.1	2.9	2.9	2.7	6.0	1.7	-	-	-	3.2	3.2
K_2O	(wt. %)	2.8	0.9	0.9	0.8	6.3	1.5	-	-	-	1.8	1.8
P_2O_5	(wt. %)	0.7	0.2	0.2	0.5	0.1	0.5	-	-	-	0.4	0.4
LOI %	(wt. %)	1.8	0.6	0.4	1.0	5.9	3.1	-	-	-	-	-

Total (majors only)[3]	(wt. %)	97.3	99.0	99.2	98.5	93.5	96.5	-	-	-	98.9	-
Total (majors+ trace oxides+LOI)[3]	(wt. %)	99.7	99.8	99.7	99.7	99.9	100.0	-	-	-	-	-
XRF Traces (RR1310 samples only)												
Ni	(ppm)	185	50.8	67.9	82.5	21.4	451	-	-	-	-	-
Cr	(ppm)	246	212	201	71.4	3.6	663	-	-	-	-	-
Sc	(ppm)	21.6	25.9	25.9	32.7	0.4	23.0	-	-	-	-	-
V	(ppm)	184	236	233	391	7.7	241	-	-	-	-	-
Ba	(ppm)	710	140	137	174	318	383	-	-	-	-	-
Rb	(ppm)	73.6	16.4	16.6	16.9	116	38.1	-	-	-	-	-
Sr	(ppm)	924	379	368	426	301	489	-	-	-	-	-
Zr	(ppm)	249	137	137	239	1032	215	-	-	-	-	-
Y	(ppm)	24.1	21.7	21.0	34.8	35.6	24.2	-	-	-	-	-
Nb	(ppm)	84.9	16.4	17.2	33.9	203	54.4	-	-	-	-	-
Ga	(ppm)	18.3	20.8	21.6	22.2	28.7	18.2	-	-	-	-	-
Cu	(ppm)	45.8	39.9	42.7	108	10.2	85.9	-	-	-	-	-
Zn	(ppm)	72.5	93.5	92.3	134	200	120	-	-	-	-	-
Pb	(ppm)	6.2	2.1	2.2	2.8	13.8	4.7	-	-	-	-	-
La	(ppm)	57.3	14.8	14.6	28.5	200	50.2	-	-	-	-	-
Ce	(ppm)	108	32.3	34.0	62.6	336	101	-	-	-	-	-
Th	(ppm)	9.7	2.1	1.3	3.0	24.8	6.3	-	-	-	-	-
Nd	(ppm)	42.7	16.8	19.7	36.0	99.8	46.1	-	-	-	-	-
U	(ppm)	3.8	2.3	0.5	1.3	1.6	3.0	-	-	-	-	-
Solution ICP Traces (RR1310, KK8203, ALIA, BCR-2)												
Cs	(ppm)	1.2	0.2	0.2	0.3	0.2	0.6	0.5	0.2	0.4	1.1	1.2
Rb	(ppm)	74.0	14.4	15.2	16.0	116.7	38.2	26.5	10.0	28.4	46.5	46.0

Ba	(ppm)	704	133	129	163	322	373	380	38	254	683	684
Th	(ppm)	10.3	1.8	1.8	2.9	26.1	6.2	8.6	1.1	5.4	6.2	5.8
U	(ppm)	2.4	0.5	0.5	0.8	1.3	1.2	1.2	0.5	1.0	1.7	1.7
Nb	(ppm)	85.5	17.1	17.1	34.8	204	55.1	98.9	10.2	57.6	11.6	12.4
Ta	(ppm)	5.4	1.2	1.2	2.4	11.3	3.3	6.8	0.7	4.0	0.8	0.8
La	(ppm)	60.6	15.0	14.8	27.2	206.5	48.1	69.0	6.3	68.7	25.7	25.1
Ce	(ppm)	107	32.9	33.0	62.0	349	97.4	136.1	12.8	126	53.5	53.1
Pb	(ppm)	5.2	1.5	1.6	1.6	14.0	4.9	7.4	2.4	8.9	10.4	10.6
Pr	(ppm)	11.9	4.4	4.4	8.4	33.9	11.6	16.3	1.7	15.7	7.0	6.8
Nd	(ppm)	43.5	18.6	18.1	37.0	105	46.2	64.2	7.3	64.2	29.2	28.3
Sr	(ppm)	944	385	375	443	305	503	296	89	286	346	337
Zr	(ppm)	259	139	139	250	1027	225	282	77	247	184	187
Hf	(ppm)	5.7	3.5	3.5	6.3	23.7	5.6	7.0	1.9	6.2	5.0	5.0
Sm	(ppm)	8.2	4.7	4.5	9.3	14.4	9.4	13.3	1.9	12.7	6.9	6.5
Eu	(ppm)	2.6	1.6	1.5	3.0	3.9	3.0	4.1	0.6	3.8	2.1	2.0
Gd	(ppm)	6.8	4.7	4.7	9.0	10.2	8.2	11.2	2.0	11.3	7.1	6.8
Tb	(ppm)	1.0	0.8	0.8	1.4	1.6	1.2	1.5	0.3	1.5	1.2	1.1
Dy	(ppm)	5.4	4.6	4.6	7.9	8.9	6.1	7.8	1.8	8.0	7.0	6.4
Ho	(ppm)	1.0	0.9	0.9	1.5	1.6	1.0	1.4	0.4	1.5	1.5	1.3
Y	(ppm)	24.5	21.9	21.4	36.0	37.3	24.6	39.0	9.5	57.1	36.2	36.1
Er	(ppm)	2.3	2.2	2.2	3.7	4.1	2.2	3.1	1.0	3.8	3.8	3.7
Tm	(ppm)	0.3	0.3	0.3	0.5	0.6	0.3	0.4	0.1	0.5	0.5	0.5
Yb	(ppm)	1.8	1.8	1.8	2.7	3.4	1.5	2.1	0.8	2.7	3.3	3.4
Lu	(ppm)	0.2	0.3	0.3	0.4	0.5	0.2	0.3	0.1	0.4	0.5	0.5
Sc	(ppm)	22.2	25.7	24.8	33.0	0.1	23.9	27.0	18.4	24.6	33.4	33.5

[1]Major elements and select trace elements for whole rock samples were measured by X-ray fluorescence (XRF) at Washington State University (WSU). These samples were analyzed together with USGS reference material BCR-2, and the BCR-2 data and preferred reference values from Jochum et al. (2016) are provided in the table. Major element data are not available for samples RR1310-D40-10, RR1310-D34-01, KK8203-DR-1, KK8203-DR-9, RR1310-D29-01, and ALIA-121-09.

[2]Trace elements for whole rock powders were analyzed by solution ICP-MS at WSU. The reference material BCR-2 was analyzed as an unknown with these samples. The new BCR-2 data are shown with the preferred values from Jochum et al. (2016). Trace element data are not available for samples RR1310-D34-01, RR1310-D29-01, and RR1310-D40-10.

[3]Two different totals are included for major element analyses. The first total includes major element oxide analyses only. The second total includes major element oxide analyses, loss on ignition (LOI), and the trace element totals expressed as oxides and includes the following trace elements: Ni, Cr, Sc, V, Ba, Rb, Sr, Zr, Y, Nb, Ga, Cu, Zn, Pb, La, Ce, Th, Nd and U.

Table 4. Major and trace element analyses of glasses examined in this study.

Sample Name		PPT-D1N1	PPT-D1N1 2RSD (%)	PPT-D1-N2	PPT-D1-N2 2RSD (%)	ALV 519-4-1	ALV 519-4-1 2RSD (%)	Preferred ALV 519-4-1 (Melson et al., 2002; Gale et al., 2013a, b)
Volcano		Papatua	-	Papatua	-	-	-	-
Material analyzed		Glass	-	Glass	-	Glass	-	-
Method of Major Element Analysis		EPMA[1] - AVG of 3	-	EPMA[1] - AVG of 3	-	EPMA[1] - AVG of 22	-	-
Method of Trace Element Analysis		LA-ICP[2] - AVG of 2	-	LA-ICP[2] - AVG of 3	-	LA-ICP[2] - AVG of 8	-	-
EPMA Majors								
SiO_2	(wt. %)	42.4	1.6	42.8	1.1	49.0	1.5	48.9
TiO_2	(wt. %)	4.1	0.4	4.1	1.3	0.7	1.3	0.8
Al_2O_3	(wt. %)	13.2	2.5	13.3	1.2	16.4	1.8	16.5
FeO_{tot}	(wt. %)	11.7	2.0	11.8	0.3	8.9	0.8	9.0
MnO	(wt. %)	0.2	4.4	0.2	2.3	0.2	5.2	-
MgO	(wt. %)	6.4	0.8	6.5	3.2	9.7	2.0	9.4
CaO	(wt. %)	13.1	1.5	13.2	2.1	12.5	0.6	12.6
Na_2O	(wt. %)	3.6	0.7	3.5	4.3	2.1	2.5	2.1
K_2O	(wt. %)	1.7	2.9	1.7	0.7	0.1	4.5	0.1
P_2O_5	(wt. %)	1.2	1.7	1.2	0.5	0.1	19.0	0.1
Total	(wt. %)	97.6	-	98.3	-	99.7	-	99.5
LA-ICP Traces (PPT glasses, ALV 519-4-1)								
Ni	(ppm)	48.9	14.9	58.6	4.2	188.8	2.6	178.0
Cu	(ppm)	68.3	17.3	63.9	6.5	107.8	2.2	98.0
Zn	(ppm)	163.8	2.1	164.4	4.1	82.9	5.5	-
Li	(ppm)	11.6	6.1	11.3	2.6	4.2	2.7	4.2

Co	(ppm)	42.9	2.6	44.5	1.8	51.2	1.5	48.7
Cs	(ppm)	0.5	2.6	0.5	5.0	0.0	44.1	0.0
Rb	(ppm)	41.0	3.0	41.1	5.1	2.1	2.2	2.0
Ba	(ppm)	633.6	2.1	615.8	1.2	24.4	2.1	24.3
Th	(ppm)	10.2	4.2	10.0	0.2	0.3	4.7	0.3
U	(ppm)	2.6	0.5	2.5	0.9	0.1	6.9	0.1
Nb	(ppm)	88.1	0.5	86.3	2.8	4.0	1.2	4.5
Ta	(ppm)	4.6	3.5	4.6	2.1	0.2	7.3	0.3
La	(ppm)	97.6	0.6	95.0	3.2	2.7	2.2	2.8
Ce	(ppm)	207.3	0.7	200.0	3.9	6.8	1.4	6.9
Pb	(ppm)	9.3	5.3	8.9	3.8	0.2	9.9	0.3
Pr	(ppm)	21.6	1.2	21.4	0.6	0.9	1.9	1.0
Nd	(ppm)	86.8	0.9	86.5	1.5	4.9	3.3	5.2
Sr	(ppm)	1183.0	4.3	1152.0	1.1	64.3	1.2	71.0
Zr	(ppm)	417.5	3.6	418.3	5.4	34.5	1.2	39.9
Hf	(ppm)	8.2	2.3	8.4	0.9	0.9	3.4	1.1
Sm	(ppm)	15.5	1.8	15.5	2.0	1.6	6.1	1.7
Eu	(ppm)	4.4	2.1	4.3	1.9	0.6	3.3	0.7
Gd	(ppm)	12.1	1.4	12.2	3.0	2.3	4.5	2.6
Tb	(ppm)	1.5	1.7	1.5	4.0	0.4	4.9	0.5
Dy	(ppm)	8.8	3.3	8.8	2.5	3.2	1.6	3.4
Ho	(ppm)	1.5	1.2	1.5	5.4	0.7	3.7	0.8
Y	(ppm)	38.5	1.8	38.9	2.7	18.6	1.7	22.3
Er	(ppm)	3.8	6.7	3.8	2.9	2.2	3.4	2.3
Tm	(ppm)	0.5	3.2	0.5	5.5	0.3	5.4	-
Yb	(ppm)	2.9	5.1	2.9	4.7	2.3	4.5	2.4
Lu	(ppm)	0.4	0.7	0.4	1.5	0.3	3.8	0.4

Sc	(ppm)	27.8	4.1	28.5	3.3	42.6	1.3	43.0

[1]Major elements on Papatua (PPT) glasses were measured by electron probe microanalyzer (EPMA) at University of California Santa Barbara (UCSB). The standard reference material ALV 519-4-1 was run together with the PPT glasses in the same analytical session and with the same instrument settings. Note that the EPMA data consist of an average of several analyses of the same sample (the number of analyses is noted at the top the data table), and the 2RSD reproducibility for multiple EPMA analyses is also provided. These data are provided with preferred values from Melson et al. (2002).

[2]Trace elements for the PPT glasses were measured by laser ablation inductively coupled plasma mass spectrometer (LA-ICP-MS) at Clermont-Ferrand along with the reference material ALV 519-4-1. These data are provided with preferred values from Melson et al. (2002) and Gale et al. (2013a, b). Note that the LA-ICP-MS data consist of an average of several analyses of the same sample (the number of analyses is noted at the top the data table), and the 2RSD reproducibility for multiple LA-ICP-MS analyses is also provided.

Table 5. Hf-Pb-Sr-Nd Isotopic Data for samples analyzed in this study [1]

Sample Name	Location	$^{176}Hf/^{177}Hf$	2SE	Hf isotopes measured at	$^{206}Pb/^{204}Pb$	2SE	$^{207}Pb/^{204}Pb$	2SE	$^{208}Pb/^{204}Pb$	2SE	Pb isotopes measured at	$^{87}Sr/^{86}Sr$	2SE	Sr isotopes measured at	$^{143}Nd/^{144}Nd$	2SE	Nd isotopes measured at
PPT-D1-N1 glass	Papatua	0.282892	0.000009	Lyon	18.6861	0.0037	15.6324	0.0030	38.8835	0.0063	Lyon	-	-	-	0.512631	0.000007	-
PPT-D1-N2 glass	Papatua	0.282877	0.000005	Lyon	18.7229	0.0003	15.6284	0.0003	38.9221	0.0008	Lyon	0.705045	0.000008	UNC	0.512622	0.000004	UNC
RR1310-D41-05	Lalla Rookh	0.283048	0.000003	Lyon	19.4521	0.0004	15.6291	0.0003	39.8335	0.0009	Lyon	0.705000	0.000008	UNC	0.512757	0.000011	UNC
RR1310-D40-10 clast	Lalla Rookh	0.282960	0.000075	Lyon	19.1582	0.0059	15.6487	0.0043	39.6997	0.0131	Lyon	0.704970	0.000010	UNC	0.512750	0.000004	UNC
RR1310-D39-01	Siafiafi	0.282977	0.000005	Lyon	19.4640	0.0006	15.6195	0.0005	39.7449	0.0015	Lyon	0.705030	0.000008	UNC	0.512792	0.000009	UNC
ALIA-D121-09 clast	Siafiafi	-	-	-	19.7439	0.0012	15.6305	0.0011	40.0489	0.0023	Lyon	-	-	-	0.512775	0.000005	UNC
ALIA-D121-09 clast rep	Siafiafi	-	-	-	-	-	-	-	-	-	-	0.704519	0.000005	UCSB	-	-	-
RR1310-D29-10	Bustard	0.283040	0.000006	Lyon	18.7645	0.0004	15.5792	0.0003	38.7311	0.0008	Lyon	0.704102	0.000010	UNC	0.512838	0.000005	UNC
	Tuscarora	0.282872	0.000004	Lyon	18.7671	0.0018	15.6655	0.0015	38.8700	0.0037	Lyon	0.707822	0.000008	UNC	0.512539	0.000005	UNC

RR1310-D34-01																
KK8203-DR-9 clast	Tuscarora	0.283112	0.000004	Lyon	18.9237	0.0004	15.5627	0.0003	38.7687	0.0008	Lyon	0.703789	0.000011	UNC	0.512921	0.000004	UNC
RR1310-D38-08	Waterwitch	0.283056	0.000004	Lyon	19.6015	0.0004	15.5979	0.0004	39.5445	0.0009	Lyon	0.703727	0.000008	UNC	0.512890	0.000004	UNC
RR1310-D38-08 rep 1	Waterwitch	-	-	-	-	-	-	-	-	-	-	0.703720	0.000005	UCSB	0.512897	0.000002	UCSB
RR1310-D38-08 rep 2	Waterwitch	-	-	-	-	-	-	-	-	-	-	0.703725	0.000006	UCSB			
KK8203-DR-1 clast	Talviuni	0.283035	0.000005	Lyon	19.0401	0.0011	15.5932	0.0007	39.4478	0.0028	Lyon	0.704271	0.000008	UNC	0.512857	0.000004	UNC
RR1310-D31-01	Fa'aitu	-	-	-	-	-	-	-	-	-	-	0.704633	0.000005	UCSB	0.512765	0.000002	UCSB
RR1310-D31-01 rep	Fa'aitu	-	-	-	18.7733	0.0031	15.5826	0.0025	38.8583	0.0066	USC	0.704642	0.000007	UCSB			-
RR1310-D31-02	Fa'aitu	-	-	-	-	-	-	-	-	-	-	0.704586	0.000006	UCSB	0.512771	0.000002	UCSB
RR1310-D31-02 rep	Fa'aitu	-	-	-	18.7650	0.0003	15.5736	0.0003	38.8240	0.0011	USC	0.704588	0.000006	UCSB	0.512765	0.000003	UCSB

USGS reference materials:

BCR-2, UCSB/USC	-	-	-	-	18.7543	0.0004	15.6188	0.0004	38.7162	0.0013	USC	0.705003	0.000006	UCSB	0.512620	0.000002	UCSB
BCR-2, UCSB/USC	-	-	-	-	-	-	-	-	-	-	-	0.705007	0.000006	UCSB	0.512621	0.000002	UCSB
BCR-2, UCSB/USC	-	-	-	-	18.7415	0.0004	15.6093	0.0004	38.6795	0.0013	USC	0.705006	0.000006	UCSB	0.512625	0.000003	UCSB
BCR-2, Lyon/UNC	-	0.282886	0.000005	Lyon	18.7588	0.0009	15.6251	0.0008	38.7414	0.0022	Lyon	0.704989	0.000010	UNC	0.512625	0.000005	UNC
BCR-2, Weis et al. 2006; 2007	-	0.282870	0.000008	-	18.7533	0.0195	15.6262	0.0040	38.7282	0.0405	-	0.705005	0.000010	-	0.512622	0.000012	-
BCR-2, avg. Woodhead and Hergt, 2000		-	-	-	18.7543	0.0110	15.6217	0.0030	38.7186	0.0210	-	-	-	-	-	-	-
AGV-2, Lyon/UNC	-	0.282989	0.000004	Lyon	18.8660	0.0009	15.6174	0.0009	38.5299	0.0032	Lyon	0.703995	0.000008	UNC	0.512769	0.000005	UNC
AGV-2, Weis et al. (2006; 2007)	-	0.282984	0.000009	-	18.8692	0.0063	15.6186	0.0071	38.5488	0.0135	-	0.703973	0.000005	-	0.512774	0.000010	-

[1]With the exception of two Papatua glasses, isotopes were measured on rock chips (not powders). The unweighted mean $^{176}Hf/^{177}Hf$ of the JMC-475 Hf standard run alternately with the samples were identical within error to the preferred value of 0.282163 ±0.000009 (Blichert-Toft et al., 1997), hence no corrections were applied to the new $^{176}Hf/^{177}Hf$ data. Isotopic compositions for all other data in the table (including previously published geologic reference materials) are normalized to an NBS987 value of 0.710240 for $^{87}Sr/^{86}Sr$, a JNdi $^{143}Nd/^{144}Nd$

value of 0.512099 (JNdi value from Garçon et al., 2018), and Pb isotopic compositions for NBS981 from Eisele et al. (2003) (i.e., $^{206}Pb/^{204}Pb$ = 16.9409, $^{207}Pb/^{204}Pb$ = 15.4976, and $^{208}Pb/^{204}Pb$ = 36.7262). Data for USGS reference materials are renormalized to preferred standard values used here (and a La Jolla to JNdi conversion from Tanaka et al. (2000) was used for $^{143}Nd/^{144}Nd$). A BCR-2 and an AGV-2 (both labeled "Lyon/UNC") were reported previously (Jackson et al., 2017; Price et al., 2017), but were analyzed together with samples reported here, so are provided in the table for completeness (but are renormalized to preferred standard values used here). Errors for sample unknowns are 2σ standard error of the mean (and represent internal precision) and are absolute (not relative). Errors on the USGS reference materials from Weis et al. (2006) represent 2SD and represent multiple analyses of a USGS reference material. Measurements in this study were made (or repeated) at a variety of institutions. We indicate when measurements were made at École Normale Supérieure Lyon (Lyon), University of South Carolina (USC), University of North Carolina, Chapel Hill (UNC), or University of California, Santa Barbara (UCSB).

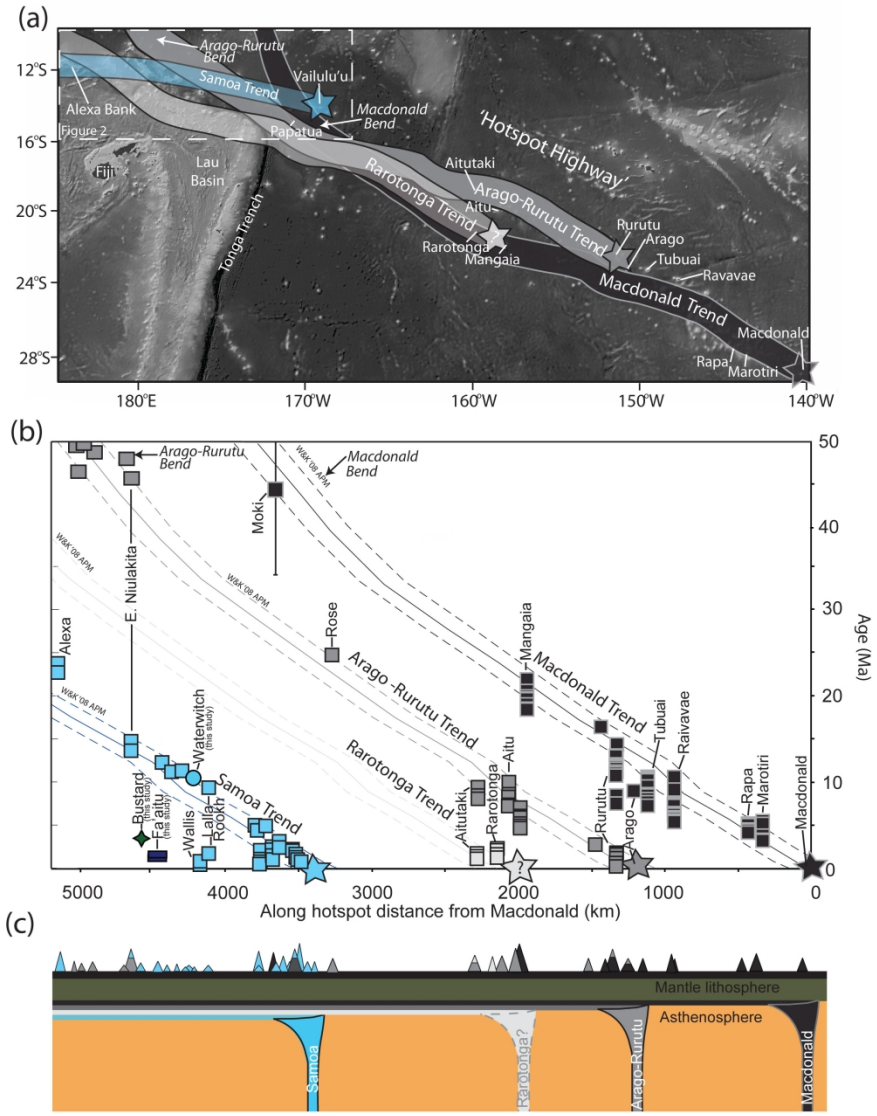

Figure 1

213x279mm (600 x 600 DPI)

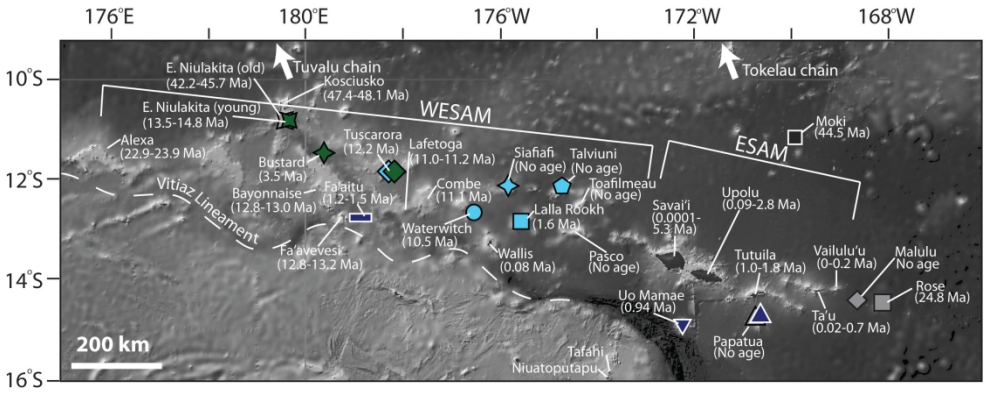

Figure 2

215x85mm (600 x 600 DPI)

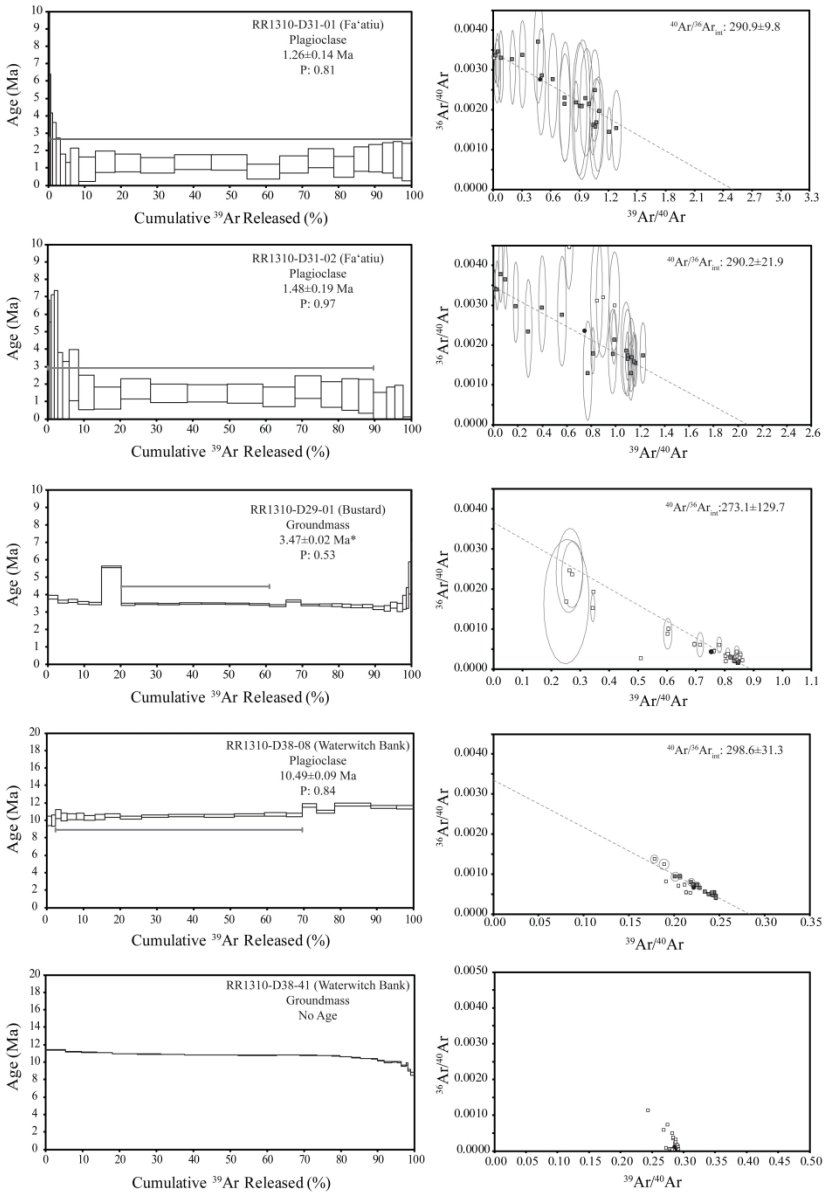

Figure 3

332x470mm (600 x 600 DPI)

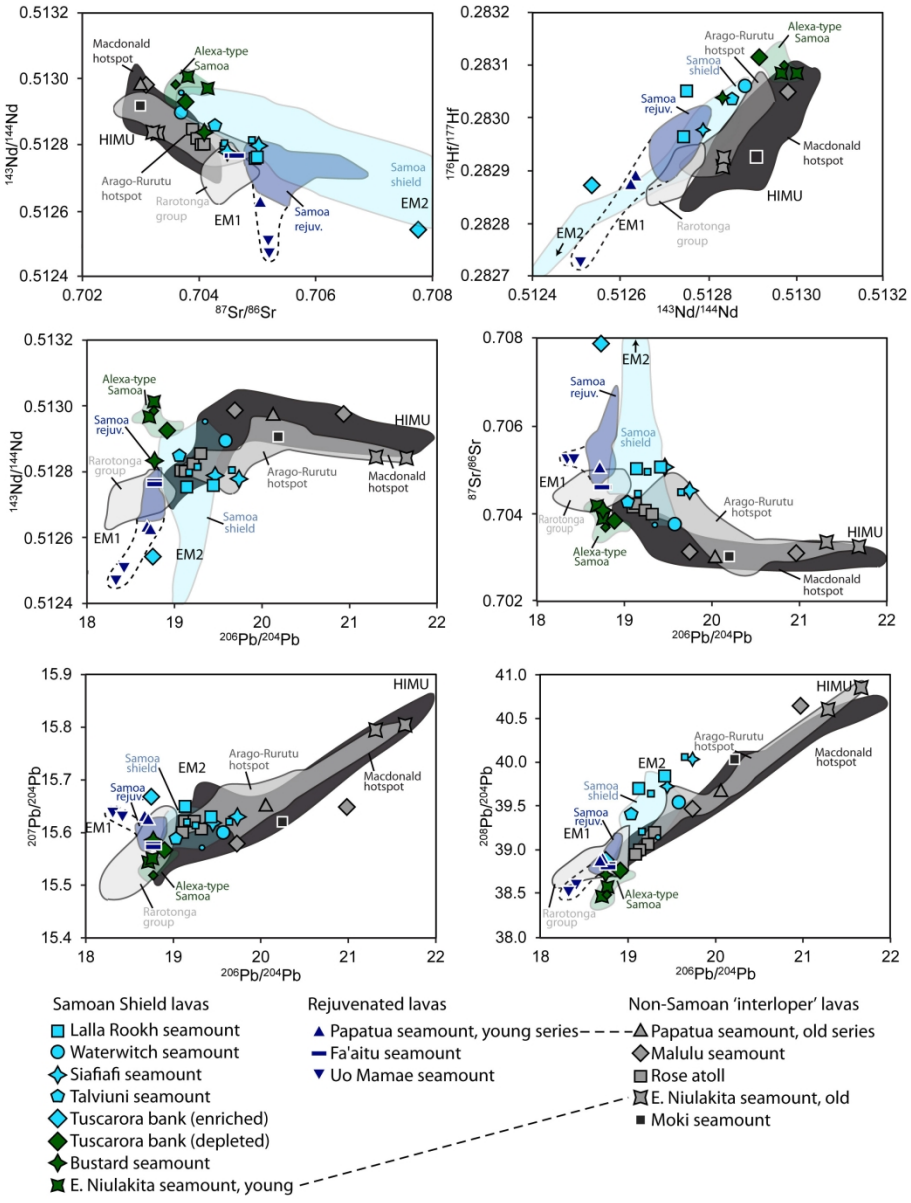

Figure 4

212x275mm (600 x 600 DPI)

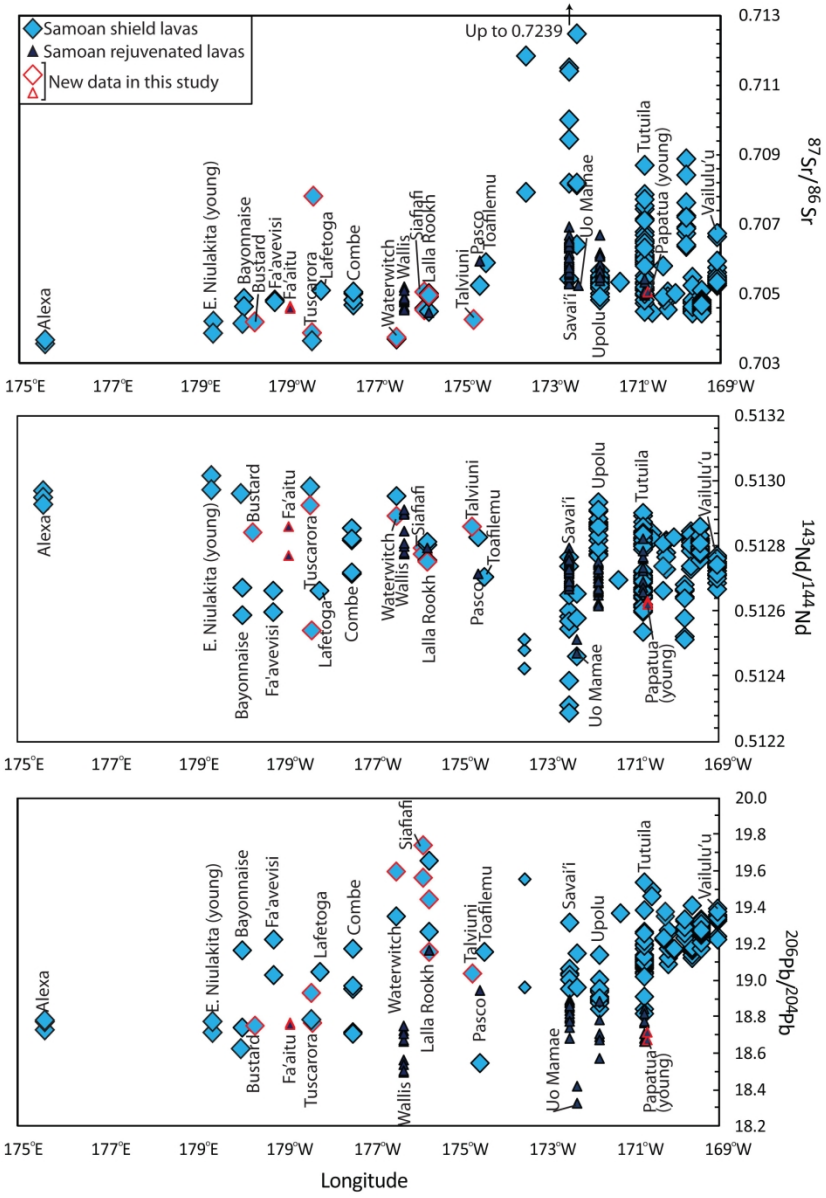

Figure 5

196x274mm (600 x 600 DPI)

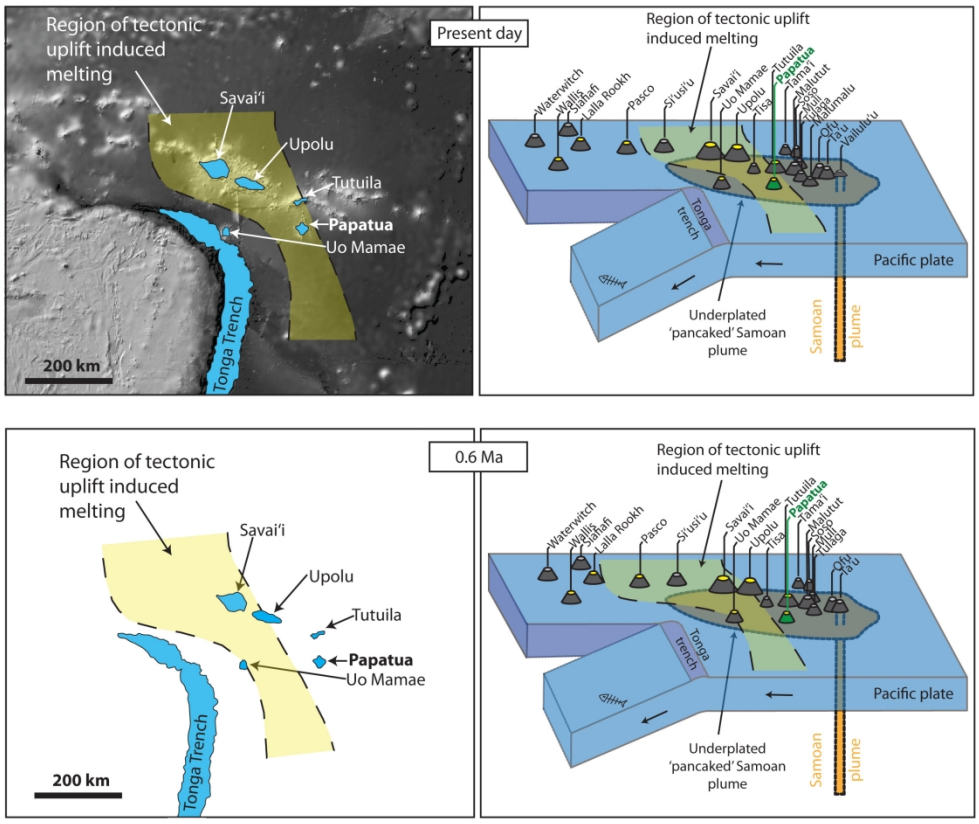

Figure 6

215x191mm (600 x 600 DPI)